The Astrophysical Journal, 572:906–931, 2002 June 20

MODELING THE *HUBBLE SPACE TELESCOPE* ULTRAVIOLET AND OPTICAL SPECTRUM OF SPOT 1 ON THE CIRCUMSTELLAR RING OF SN 1987A[1]

Chun S. J. Pun,[2,3,4] Eli Michael,[5] Svetozar A. Zhekov,[5,6] Richard McCray,[5] Peter M. Garnavich,[7] Peter M. Challis,[8] Robert P. Kirshner,[8] E. Baron,[9] David Branch,[9] Roger A. Chevalier,[10] Alexei V. Filippenko,[11] Claes Fransson,[12] Bruno Leibundgut,[13] Peter Lundqvist,[12] Nino Panagia,[14] M. M. Phillips,[15] Brian Schmidt,[16] George Sonneborn,[3] Nicholas B. Suntzeff,[17] Lifan Wang,[18] and J. Craig Wheeler[19]

Received 2001 December 12; accepted 2002 February 28

ABSTRACT

We report and interpret *Hubble Space Telescope* (*HST*) Space Telescope Imaging Spectrograph (STIS) long-slit observations of the optical and ultraviolet (1150–10270 Å) emission line spectra of the rapidly brightening spot 1 on the equatorial ring of SN 1987A between 1997 September and 1999 October (days 3869–4606 after outburst). The emission is caused by radiative shocks created where the supernova blast wave strikes dense gas protruding inward from the equatorial ring. We measure and tabulate line identifications, fluxes, and, in some cases, line widths and shifts. We compute flux correction factors to account for substantial interstellar line absorption of several emission lines. Nebular analysis shows that optical emission lines come from a region of cool ($T_e \approx 10^4$ K) and dense ($n_e \approx 10^6$ cm^{-3}) gas in the compressed photoionized layer behind the radiative shock. The observed line widths indicate that only shocks with shock velocities $V_s < 250$ km s^{-1} have become radiative, while line ratios indicate that much of the emission must have come from yet slower ($V_s \lesssim 135$ km s^{-1}) shocks. Such slow shocks can be present only if the protrusion has atomic density $n \gtrsim 3 \times 10^4$ cm^{-3}, somewhat higher than that of the circumstellar ring. We are able to fit the UV fluxes with an idealized radiative shock model consisting of two shocks ($V_s = 135$ and 250 km s^{-1}). The observed UV flux increase with time can be explained by the increase in shock surface areas as the blast wave overtakes more of the protrusion. The observed flux ratios of optical to highly ionized UV lines are greater by a factor of ~2–3 than predictions from the radiative shock models, and we discuss the possible causes. We also present models for the observed Hα line widths and profiles, which suggest that a chaotic flow exists in the photoionized regions of these shocks. We discuss what can be learned with future observations of all the spots present on the equatorial ring.

Subject headings: circumstellar matter — supernova remnants — supernovae: individual (SN 1987A)

1. INTRODUCTION

SN 1987A in the Large Magellanic Cloud provides an unprecedented opportunity to observe the birth and development of a supernova remnant (SNR). *International Ultraviolet Explorer* (*IUE*) observations (Fransson et al. 1989; Sonneborn et al. 1997) found narrow line emission about 80 days after the explosion,[20] demonstrating the presence of circumstellar gas around SN 1987A. Images taken with the *Hubble Space Telescope* (*HST*) showed that this gas consists of an equatorial inner ring (radius ≈0.7 lt-yr, $n_e \sim 3 \times 10^3$ to 3×10^4 cm^{-3}) and two outer rings (~3 times the size of the inner ring, $n_e \lesssim 2000$ cm^{-3}) tilted toward the observer at ~45° (Jakobsen et al. 1991; Wang 1991; Plait et al. 1995; Burrows et al. 1995; Lundqvist & Fransson 1996; Maran et al. 2000; Lundqvist & Sonneborn 2001). The circumstellar ring system was excited by the ionizing radiation from the supernova during the shock breakout (Lundqvist &

[1] Based on observations with the NASA/ESA *Hubble Space Telescope*, obtained at the Space Telescope Science Institute, which is operated by the Association of Universities for Research in Astronomy, Inc., under NASA contract NAS 5-26555.

[2] NASA Goddard Space Flight Center, Laboratory for Astronomy and Space Physics, Code 681, Greenbelt, MD 20771.
[3] National Optical Astronomical Observatories, P.O. Box 26732, Tucson, AZ 85726.
[4] Present address: Department of Physics, Hong Kong University, 518 Chong Yuet Ming Physics Building, Pokfulam Road, Hong Kong, China; jcspun@hkucc.hku.hk.
[5] JILA, University of Colorado, Boulder, CO 80309-0440.
[6] On leave from Space Research Institute, Sofia, Bulgaria.
[7] Department of Physics, University of Notre Dame, 225 Nieuwland Science Hall, Notre Dame, IN 46556.
[8] Harvard-Smithsonian Center for Astrophysics, 60 Garden Street, Cambridge, MA 02138.
[9] Department of Physics and Astronomy, University of Oklahoma, 440 West Brooks Street, Norman, OK 73019.
[10] Department of Astronomy, University of Virginia, P.O. Box 3818, Charlottesville, VA 22903.
[11] Department of Astronomy, University of California, Berkeley, CA 94720-3411.
[12] SCFAB, Stockholm Observatory, Department of Astronomy, SE-10691 Stockholm, Sweden.
[13] European Southern Observatory, Karl-Schwarzschild-Strasse 2, D-85784 Garching, Germany.
[14] Space Telescope Science Institute, 3700 San Martin Drive, Baltimore, MD 21218; on assignment from the Space Science Department of ESA.
[15] Carnegie Institution of Washington, Las Campanas Observatory, Casilla 601, La Serena, Chile.
[16] Mount Stromlo and Siding Spring Observatories, Private Bag, Weston Creek PO, Canberra, ACT 2611, Australia.
[17] Cerro Tololo Inter-American Observatory, Casilla 603, La Serena, Chile.
[18] Institute for Nuclear and Particle Astrophysics, E. O. Lawrence Berkeley National Lab, Berkeley, CA 94720.
[19] Department of Astronomy, University of Texas, Austin, TX 78712.

[20] The time of core collapse of SN 1987A, 1987 February 23.316 UT (JD = 2,446,849.816), was determined by the IMB and Kamiokande II neutrino detectors (Bionta et al. 1987; Hirata et al. 1987).

Fransson 1991; Ensman & Burrows 1992; Blinnikov et al. 2000). In the interacting winds model, the SN 1987A ring system is part of a bipolar shell around the supernova (Blondin & Lundqvist 1993; Martin & Arnett 1995; Link, Rosenberg, & Chevalier 2002).

The first signal of ongoing interaction between the SN 1987A debris and the circumstellar gas was the rebirth of the supernova in X-ray (Beuermann, Brandt, & Pietsch 1994; Gorenstein, Hughes, & Tucker 1994; Hasinger, Aschenbach, & Trümper 1996) and radio (Staveley-Smith et al. 1992, 1993) wavelengths around day 1000. The size of the radio-emitting region indicated that the supernova debris expanded unimpeded at velocity $\gtrsim$35,000 km s^{-1} up to approximately day 1000 before slowing down to $\approx$3500 km s^{-1} by the interaction (Gaensler et al. 1997; Manchester et al. 2002). The X-ray and radio observations have been explained as the interaction of the supernova ejecta with a rather dense ($n_{\rm H} \approx 100$ cm^{-3}) H II region that separates the shocked stellar wind of the supernova progenitor from the denser gas of the inner ring (Chevalier & Dwarkadas 1995; Borkowski, Blondin, & McCray 1997a).

The "main event" of the birth of SNR 1987A—the interaction between the supernova debris and the circumstellar rings—has been anticipated since the discovery of the circumstellar gas. Predictions of the time of the first contact ranged from 2003 (Luo & McCray 1991) to 1999 ± 3 (Luo, McCray, & Slavin 1994) to 2005 ± 3 (Chevalier & Dwarkadas 1995). There have been previous model predictions of radiation from this impact in X-rays (Suzuki, Shigeyama, & Nomoto 1993; Masai & Nomoto 1994; Borkowski, Blondin, & McCray 1997b) and in the UV/optical (Luo et al. 1994). The first definitive sign of impact between the supernova blast wave and the inner ring was detected in the 1997 April *HST* Space Telescope Imaging Spectrograph (STIS) spectral images as a blueshifted (about -250 km s^{-1}) Hα feature at P.A. $\approx 30^\circ$ of the ring (Sonneborn et al. 1998). Subsequent analysis of the *HST* Wide Field and Planetary Camera 2 (WFPC2) images taken in 1997 July showed that a point emission, located in projection at 88% of the distance to the ring, was increasing in brightness over a wide range of wavelengths (Garnavich, Kirshner, & Challis 1997; Garnavich et al. 2001) and could be traced back to as early as 1995 March (day 2932; Lawrence et al. 2000a). The position of the brightening spot, located just inside the edge of the inner ring, suggested that this is the result of an interaction of the supernova blast wave with an inward protrusion of the ring. This brightening spot, named spot 1, has increased in flux by a factor of $\sim$10 between 1996 and 1999 (Garnavich et al. 2001). With a number of new spots ($\sim$10 in 2000 November) since then detected all around the inner circumstellar ring (Garnavich, Kirshner, & Challis 2000; Lawrence et al. 2000a), we are now witnessing the full birth of SNR 1987A.

We present here *HST*/STIS UV and optical spectroscopy of spot 1 taken by the Supernova INtensive Study (SINS) collaboration up to day 4606 (1999 October 7). Results from an earlier (day 3869, 1997 September 27) STIS spectrum of spot 1 have been presented in Michael et al. (2000). We describe the new observations and data reduction in § 2 and report the results in § 3. In § 2.3 we describe a detailed method to determine the intrinsic fluxes and widths of a few UV lines, including the Si IV $\lambda\lambda$1394, 1403 and C IV $\lambda\lambda$1548, 1551 doublets, which are strongly affected by interstellar line absorption along the line of sight to the supernova.

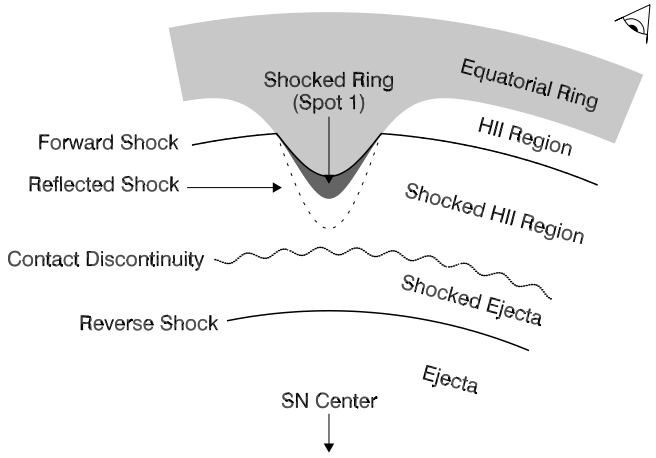

FIG. 1.—Schematic representation of the double-shock structure of SNR 1987A.

Our working model (Fig. 1) for spot 1, as well as the other spots, is that it is caused by the impact of the supernova blast wave with a dense inward protrusion of the ring (Michael et al. 2000). When the blast wave overtakes such an obstacle, slower shocks are transmitted into it. Since a range of densities is present in the ring, we expect (§ 4.1) that the transmitted shocks will have a range of velocities ($V_s \sim$ 100–1000 km s^{-1}). Not all of these shocks are responsible for the observed UV/optical emission from spot 1 though. While some UV and optical line emission is produced right at the shock front, a much larger amount is produced if the shocked gas undergoes thermal collapse, i.e., the shock becomes radiative (§ 4.2). The time it takes for a shock to make this transition increases with its speed and decreases with its preshock density. Once the postshock gas collapses, a shock becomes an extremely efficient radiator of UV and optical emission lines (§ 4.3). Therefore, while the range of possible velocities present in the ring is large, we are only observing the shocks that are slow and/or dense enough to have become radiative. Michael et al. (2000) confirmed this general picture and found that the observed line widths and line intensity ratios indicated that the emission was formed by radiative shocks in the velocity range $\sim$100–250 km s^{-1} entering into a dense ($n_0 \gtrsim 10^4$ cm^{-3}) gas.

Nebular analysis of the observed emission lines of spot 1 (§ 5.1) suggests that the emission comes from a region of high density ($n_e > 10^6$ cm^{-3}). This result confirms our picture that this emission comes from radiative shocks, which can compress the preshock gas by a factor $\gtrsim$100. In § 5.2 we model the UV line fluxes from spot 1 between day 3869 and day 4587 with the one-dimensional steady state shock code of Cox & Raymond (1985). The observed UV fluxes are fitted well with models containing emission from two radiative shocks with $V_s = 135$ and 250 km s^{-1}. We propose two scenarios to interpret the observed increase of UV flux with time of spot 1. In the first scenario the density of the obstacle is low enough so that the cooling times of shocks entering the obstacle are comparable to the age of the spot. The increase in UV line fluxes is then due primarily to the aging of the shocks as they develop thermally collapsed layers. In the second scenario, the obstacle is dense enough so that all

the shocks cool almost immediately. The increased observed fluxes are instead attributed to an increasing surface area of shock interaction. While the second scenario fits the observed fluxes better, we suspect that the actual light curves probably manifest a combination of both effects. In § 5.3 we discuss the observed line profiles and present simulated Hα line profiles based on simple geometric models for the shock interaction. In § 6 we discuss what we have learned by comparing results of simplified shock models with the spectral observations and describe how future observations may elucidate some unsolved problems. We summarize the main results in § 7.

2. OBSERVATIONS AND DATA REDUCTION

The STIS observations of spot 1 in both optical and UV wavelengths obtained by the SINS team are listed in Table 1. SN 1987A is located in a densely populated region of the LMC and appears to belong to a loose, young cluster region (Panagia et al. 2000). Target acquisition was complicated by the stars present near the supernova, especially star 3, a Be star of $V \sim 16$, at 1.″63 away and P.A. = 118°, and star 2, a B2 III star of $V = 15.0$, at 2.″91 away and P.A. = 318° from the supernova (Walborn et al. 1993; Scuderi et al. 1996). We decided to peak up on the nearby star S2 (Walker & Suntzeff 1990) and offset the telescope to center the aperture on spot 1. We measured the required offset from the WFPC2 images (Garnavich et al. 2001). Because of the uncertainties in this measurement, spot 1 was located at 0.″08 off the center of the slit for all observations taken before 1999 August. We reduced these data using the standard calibration files, which assumed that the object was located at the center of the slit. We estimate that the offset from the center of the slit will cause us to underestimate the measured flux by $\lesssim 5\%$ for the 0.″2 data and by $\lesssim 0.1\%$ for the 0.″5 data.

With each grating setting, we took multiple (three to five) observations centered at dithered positions 0.″5 apart along the slit. Cosmic rays (in the case of optical data) and hot pixels (in optical and UV data) were removed simultaneously when the dithered raw images were combined with the CALSTIS software developed by the STIS Investigation Definition Team at the Goddard Space Flight Center.[21] Previous narrow-slit STIS spectra processed by the SINS team with this software showed that the flux calibration of far-UV (G140L) and near-UV (G230L) data agrees to $\lesssim 2\%$ for the overlapping region, while the agreement between near-UV (G230L) and optical (G430L) data is good to $\lesssim 5\%$ (Baron et al. 2000; Lentz et al. 2001).

The location and orientation of the aperture positions are shown in Figure 2. For all but one of the observations, the slit was oriented (within ±5°) along the axis connecting the center of the SN 1987A debris and spot 1, which is located at P.A. = 29° on the inner ring (Garnavich et al. 2001). The only exception was the 1999 October G140L observation (Fig. 2*b*), where the (52″ × 0.″2) slit had a P.A. of 55° and did not pass through the center of the SN 1987A debris. In all observations, the spot 1 spectrum overlapped with that from the adjacent segment of the inner circumstellar ring that was included within the STIS aperture. With an expansion velocity of 10.5 ± 0.3 km s^{-1} (Cumming & Lundqvist 1997; Crotts & Heathcote 2000), the ring was not resolved spectrally in any of the STIS observations reported here. In the optical data, the emission from the ring is the main source of background to the spot 1 spectrum and will be discussed in §§ 2.1 and 2.2.

Garnavich et al. (2001) measured the width of spot 1 in WFPC2 images up to 1999 April 21 (day 4440) and showed that spot 1 was unresolved in the data and was consistent with a point source at optical wavelengths. We compared the FWHM of spot 1 emissions in our last STIS observations from 1999 September with those of point sources that were recorded in the data. We found that the FWHM of spot 1 was $8\% \pm 6\%$ and $25\% \pm 9\%$ larger than a point source in the far-UV and optical wavelengths, respectively. The latter result is consistent with measurements by Lawrence, Sugerman, & Crotts (2000b) with the 2000 May 1 (day 4816) STIS G750M spectroscopy, which suggests that spot 1 is now moderately resolved in the *HST* data at optical wavelengths.

2.1. *Low-Resolution Optical Observations*

We extracted the low-resolution optical spectrum of spot 1 from the STIS G430L and G750L two-dimensional spectral images. Portions of the 1999 September G430L and G750L data taken with the 0.″2 slit are shown in Figures 3*c* and 3*d*, respectively. The horizontal streaks near the center of the panels are broad emission lines from the inner supernova debris, which have an FWHM velocity $v_{\rm FWHM} \approx 2800$ km s^{-1} (Wang et al. 1996; Chugai et al.

[21] The CALSTIS Reference Guide is available at http://hires.gsfc.nasa.gov/stis/software/doc_manuals.html.

TABLE 1
HST/STIS Observations of Spot 1

Grating Setting	Slit (arcsec)	Wavelength Range (Å)	Resolution (Å)	Date	Days after Outburst	Exposure Time (s)
G140L (1425).....	52 × 0.5	1140–1700	1.0	1997 Sep 27	3869.3	11222
G140L (1425).....	52 × 0.5	1140–1700	1.0	1999 Feb 27	4387.6	14350
G140L (1425).....	52 × 0.2	1140–1700	1.0	1999 Oct 7	4606.1	10478
G230L (2376).....	52 × 0.2	1570–3180	3.0	1999 Sep 17	4586.5	10125
G430L (4300).....	52 × 0.2	2900–5700	4.0	1999 Sep 3	4571.9	7583
G750L (7751).....	52 × 0.5	5240–10270	8.0	1999 Feb 21	4380.9	10500
G750L (7751).....	52 × 0.2	5240–10270	8.0	1999 Sep 18	4387.4	7583
G750M (6581)....	52 × 0.2	6295–6867	1.0	1998 Mar 7	4030.0	8056
G750M (6581)....	52 × 0.1	6295–6867	1.0	1999 Aug 30	4368.0	3 × 7804[a]

[a] Not all observations centered on spot 1 (refer to text).

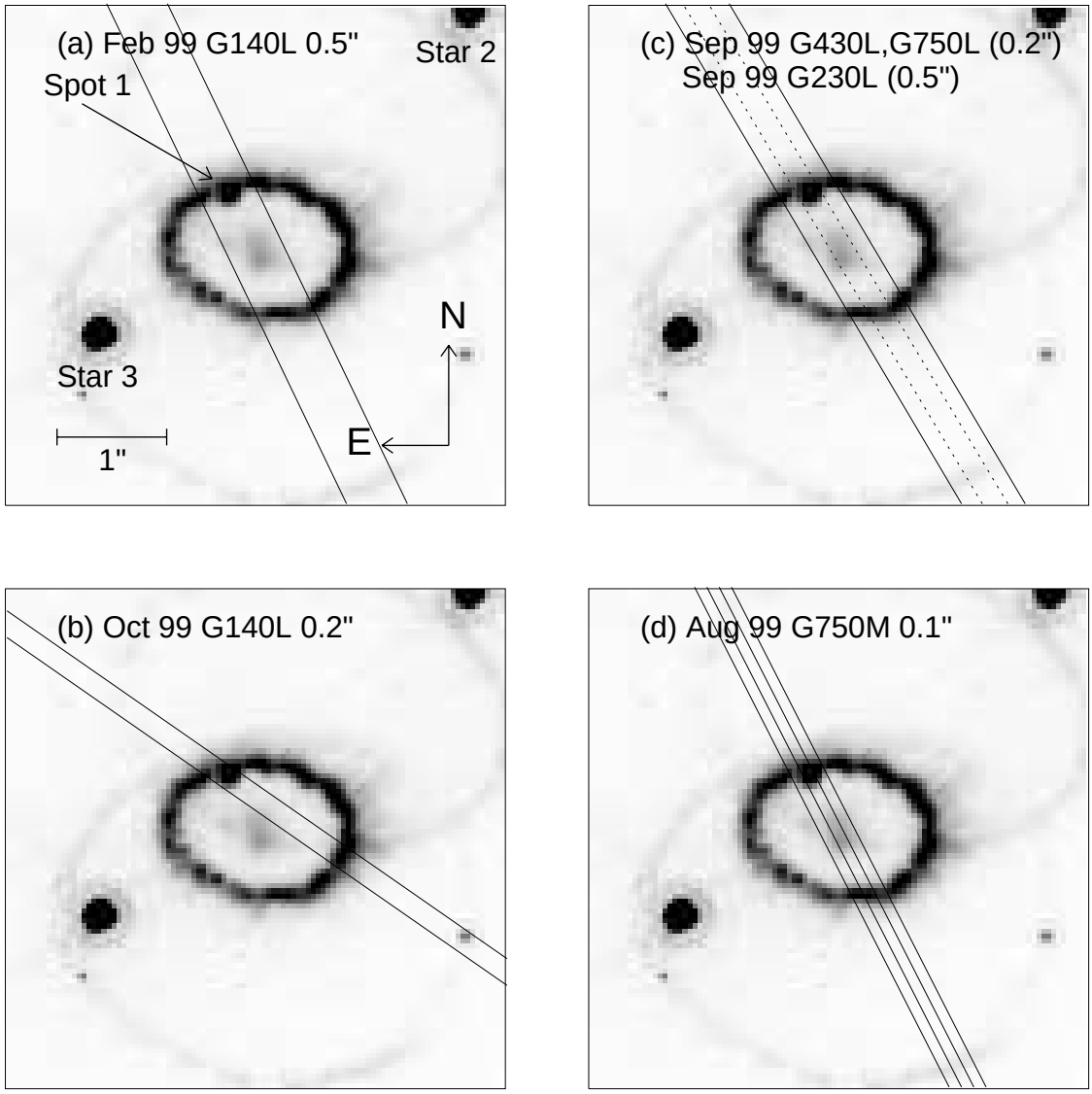

FIG. 2.—(*a*) Slit position of 1999 February 27 G140L 0.″5 observation plotted on the 1999 April 21 WFPC2 Hα image of SN 1987A. The image displayed is a 4.″56 × 4.″56 square. (*b*) Same as (*a*), but for the 1999 October 7 G140L 0.″2 observation. (*c*) Same as (*a*), but for the 1999 September 17 G230L observation (*solid lines*) and for the 1999 September 3 G430L and 1999 September 18 G750L 0.″2 observations (*dotted lines*). (*d*) Same as (*a*), but for the 1999 August 30 G750M 0.″1 observations. All three 0.″1 slit positions are plotted.

1997). For these data, the lower section of the spectral image is the combined spot 1 and inner ring emission-line spectrum (hereafter referred to as the spot 1+north ring, or S1+NR, spectrum). At the kinematic resolution of the G430L and G750L grating settings ($\Delta V \approx 300$–550 km s^{-1}), neither the emission lines from spot 1 ($v_{\rm FWHM} \approx 200$ km s^{-1}; Michael et al. 2000) nor those from the ring ($v_{\rm FWHM} \simeq 10$ km s^{-1}) are resolved. The upper section of the spectral image is the emission-line spectrum of the segment of the inner ring subsection that is in the slit and directly opposite that of spot 1 (hereafter referred to as the south ring, or SR, spectrum).

We measured the S1+NR and SR spectra in the G430L and G750L grating settings by integrating the seven to nine rows of the image in which the emission-line spectra appeared. Emissions due to the diffuse LMC background in the Balmer lines, [O II] $\lambda\lambda$3727, 3729, and [O III] $\lambda\lambda$4959, 5007 are observed as images of the entire slit at those wavelengths in Figures 3*c* and 3*d*. We subtracted the contribution of this diffuse emission from the spot 1 spectrum by linear interpolation above and below the extracted rows. Since the subtracted LMC background was only a small fraction of the emission from spot 1 (<2% for [O III] λ5007), this subtraction did not significantly increase the uncertainty of the estimated line fluxes.

We measured the flux of each emission line in the S1+NR and SR spectra by fitting a Gaussian to the line profile, allowing the net flux, width, and central wavelength to vary independently for each line. We estimated the background level from a linear fit over a 45 pixel region of the spectrum centered on the line in question but excluding any emission-line features. We fitted the line flux by minimizing the total χ^2 in which the coefficients defining the line and the background were free parameters. Gaussian profiles gave satisfactory fits to all the line profiles. The reduced χ^2, or χ^2_r (the total χ^2 divided by the number of degrees of freedom), of our line fits were within the range 0.8–2.8, compared to the

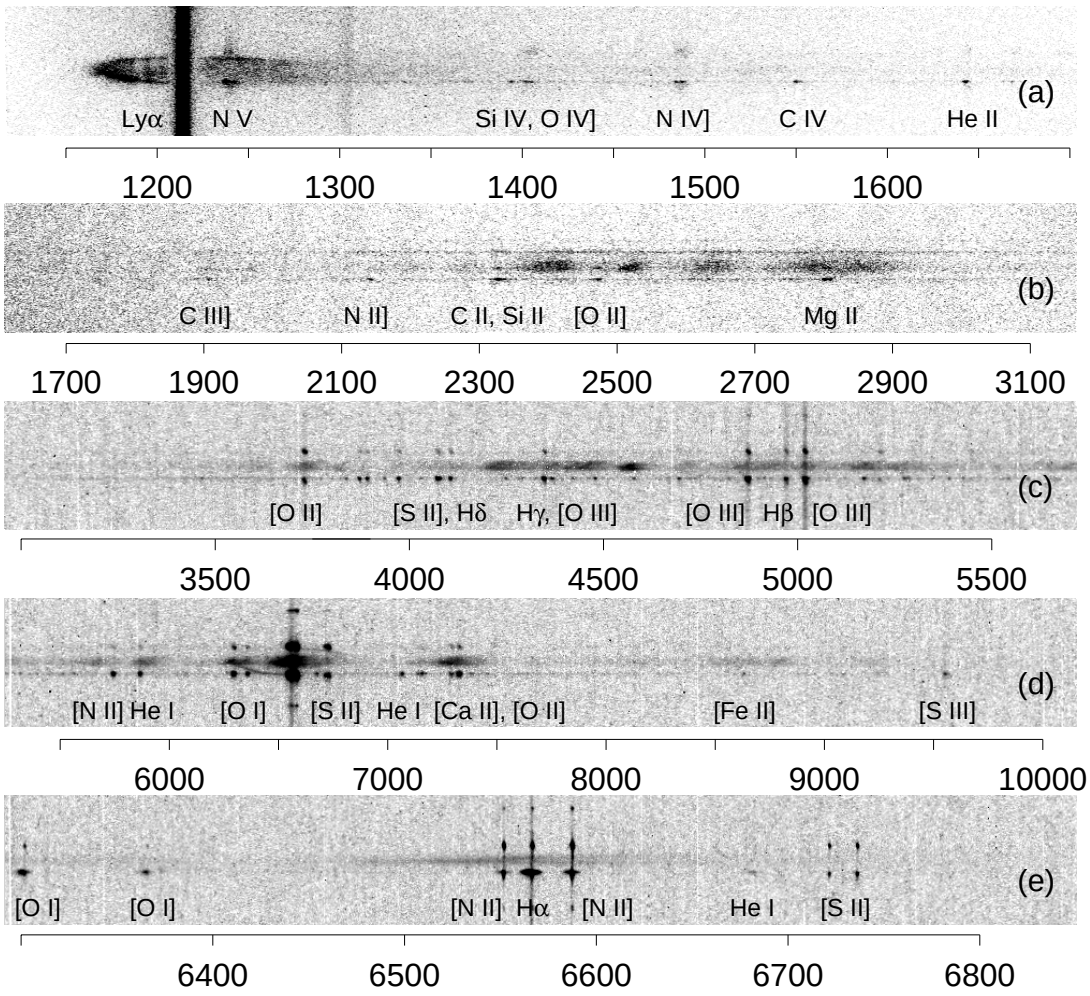

FIG. 3.—(*a*) Subsection of the 1999 October 7 STIS G140L (1425) spectral image showing the emission from spot 1. The height of the image displayed is 6″ along the slit. (*b*) Same as (*a*), but for the 1999 September 17 STIS G230L (2376) data. (*c*) Same as (*a*), but for the 1999 September 3 STIS G430L (4300) data. (*d*) Same as (*a*), but for the 1999 September 18 STIS G750L (7751) data. (*e*) Same as (*a*), but for the 1999 August 30 STIS G750M (6581) data.

value of 1.0 for a statistically good fit. We computed the flux of each line and its error from the best-fit parameters and their associated uncertainties. We adjusted the statistical errors of all the line fluxes so that $\chi_r^2 = 1.0$ for all fits. In cases in which two or more emission lines overlapped in wavelength, such as [O III] λ5007 + He I λ5016 and [Ar III] λ7136 + [Fe II] $\lambda\lambda$7155, 7172, we fitted the emission features with multiple Gaussians with the additional constraint that their wavelength separations were the known differences of laboratory wavelengths.

Only a subset $\left(\sim\frac{1}{3}\right)$ of the emission lines observed in the S1+NR spectrum also appeared in the SR spectrum. Therefore, we attributed entirely to spot 1 the measured fluxes of emission lines that were seen in the S1+NR spectrum but not in the SR one. To subtract the NR spectrum from the S1+NR spectrum, we assumed that the fluxes of emission lines in the NR spectrum are equal to those in the SR spectrum scaled by factors that are independent of time. This assumption is reasonable because the rate of flux decrease around the ring has been shown to be relatively constant around the ring (Plait et al. 1995; Lundqvist & Sonneborn 2001). We estimated the scale factors by examining archival WFPC2 emission-line images in Hα, [O III] λ5007, and [N II] λ6583 obtained in 1994 February and 1994 September, before spot 1 appeared. We measured flux ratios f(NR)/f(SR) of 1.2, 1.1, and 1.3, respectively, from the Hα, [O III] λ5007, and [N II] λ6583 images. We used the Hα scale factor for the Balmer lines. While we used the [O III] λ5007 factor for the [O III] $\lambda\lambda$4363, 4959, 5007 lines and likewise for the [N II] lines, we recognized the increase in systematic errors in the measured spot 1 fluxes of [O III] λ4363 and [N II] λ5755 because these lines are more temperature sensitive than the other lines. For all remaining emission lines, such as [S II] and [Ne III], we assumed a scale factor of 1.2 ± 0.1 in order to subtract the NR spectrum.

In addition to the 0″.2 data sets described above, we obtained one observation of spot 1 with the 0″.5 slit and the G750L grating setting. As before, we extracted the combined S1+NR spectrum by integrating the six rows of the image where the emission lines appeared. For the emission lines produced predominantly by spot 1, such as He I λ6678 and [Ar III] λ7135, we measured the S1 fluxes by fitting the line emissions with single-Gaussian profiles. For the lines where emission from S1+NR was apparent, such as [N II] λ5755 and [O I] λ6300, we estimated the contribution of the NR flux to the S1+NR flux from a linear interpolation of the NR emission-line flux adjacent to spot 1 in the slit. After subtracting this background, we fitted the remaining S1

emission lines with Gaussian profiles. The uncertainties in the background ring flux estimated in this procedure resulted in larger systematic errors in the estimated spot 1 line fluxes for this observation.

2.2. *Medium-Resolution Optical Observations*

A medium-resolution optical spectrum was taken on 1999 August 30 (UT, 4368.0 days since explosion) with a 0.″1 slit and the G750M (6581) grating setting (6295–6867 Å). With a spectral resolution of $\Delta V \simeq 50$ km s^{-1}, emission lines from spot 1, with $v_{\rm FWHM} \approx 200$ km s^{-1} (Michael et al. 2000), were resolved in the data, while the emission from the unshocked inner ring, with $v_{\rm FWHM} \simeq 10$ km s^{-1}, remained unresolved. Three observations of 7800 s each were taken at three parallel slit positions, pointed so that the middle slit position was centered on spot 1 and the two other slit positions were immediately adjacent (see Fig. 2*d*). Therefore, the observation covered a segment of the ring of length 0.″3.

With the crowded stellar field near SN 1987A, we did not execute the acquisition peak-up exposure for these 0.″1 slit observations as suggested by the *HST*/STIS operation manual (Leitherer et al. 2000). Instead, all three adjacent slit positions were placed on spot 1 by blind offsets. Therefore, we cannot apply the standard pipeline data reduction procedures to process these data. To determine the fluxes of emission lines from spot 1, we first removed the wavelength-dependent aperture throughput correction function in the pipeline data for each 0.″1 slit spectrum. We then summed the fluxes from the three 0.″1 slit positions and multiplied the total flux by a new aperture correction function for an equivalent 0.″3 slit, calculated by interpolating the pipeline corrections for the 0.″1, 0.″2, and 0.″5 slits. For Hα, the aperture correction led to a $\simeq$20% decrease of flux over the sum of the fluxes measured in the three slit positions. We calculated the corresponding 1 σ errors by combining the individual errors in quadrature.

A section of the spectral image from the middle slit position is shown in Figure 3*e*. Again, the central horizontal streak is emission from the SN 1987A debris. Emissions from the inner ring at the two positions where the ring intersected with the slit aperture were observed in [O I] $\lambda\lambda$6300, 6364, Hα, [N II] $\lambda\lambda$6548, 6583, and [S II] $\lambda\lambda$6717, 6731. In the lower section of the spectral image, emission from the stationary inner ring overlapped with the broadened emission from spot 1. Again, the major source of contamination in the spot 1 spectrum is the emission from the inner circumstellar ring within the 0.″1 slit. As described by Michael et al. (2000), we fit all the spot 1 emission features with Gaussian functions. Emission from the stationary ring dominated the spectral profile near zero velocity (approximately $\pm$50 km s^{-1}) and was excluded from the fit. The majority of the line profiles could be fitted well with Gaussian profiles, such as the fit to the [N II] λ6583 line emission shown in Figure 4. The sole exception was the Hα line profile, where the signal was strong enough to show noticeable departures from a Gaussian profile, as we shall discuss further in § 5.3.

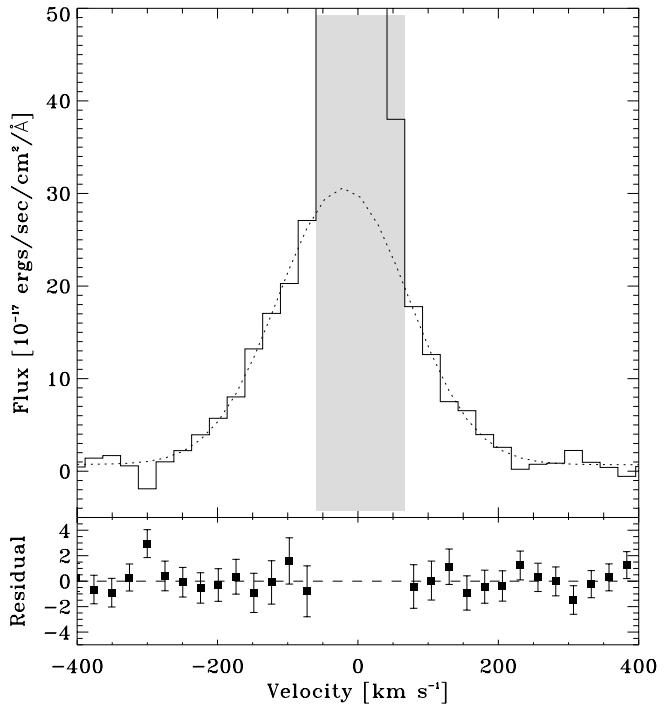

FIG. 4.—Profile of the [N II] λ6583 spot 1 emission obtained with the G750M (6581) grating in 1999 August. The low-velocity region (*shaded*) was dominated by emission from the circumstellar ring and was excluded from the fit. The best-fit Gaussian (*dotted line*) to the spot 1 emission is shown. The velocity scale has been corrected for the heliocentric velocity of the LMC (285 km s^{-1}). The residual to the best-fit Gaussian is also shown.

2.3. *Low-Resolution UV Observations*

We obtained low-resolution UV spectra of spot 1 with the G140L and G230L grating settings. Michael et al. (2000) have already presented results from the first G140L far-UV observations in 1997 September 27 taken with the 0.″5 slit. We detected emission lines from spot 1 in N V $\lambda\lambda$1239, 1243, Si IV $\lambda\lambda$1394, 1403, O IV] λ1400, N IV] $\lambda\lambda$1483, 1487, C IV $\lambda\lambda$1548, 1551, and He II λ1640. We detected the same set of emission lines in 1999 February 27, observing again with the 0.″5 slit. In 1999 October 7, observing with the 0.″2 slit, we also detected the C II λ1335 multiplet, [Ne IV] λ1602, and O III] $\lambda\lambda$1661, 1666. Figure 3*a* shows a section of the spectral image from this observation. Radiation from spot 1 is evident in the lower portion of the image, whereas only faint line emission from the inner circumstellar ring can be seen in the upper half of the displayed image. The broad (approximately $\pm$15,000 km s^{-1}) Lyα radiation comes from the reverse shock from the interaction between the supernova debris and the H II region located inside of the equatorial ring (Sonneborn et al. 1998; Michael et al. 1998a, 1998b). Fluxes of UV line emission from the inner ring are much less than those from spot 1 and make a negligible contribution to the measured fluxes. This is also the case for the near-UV emission lines measured in the 1999 September 17 G230L 0.″2 observation, shown in Figure 3*b*.

We measured the far-UV and near-UV spectra of spot 1 from the G140L and G230L data, respectively, by procedures similar to those described in § 2.1. We fitted emission lines with Gaussian profiles and linear backgrounds, except for the broad Lyα emission underlying the N V $\lambda\lambda$1239, 1243 doublet, which we fitted with a quadratic function. We fitted the two components of close doublets such as N V $\lambda\lambda$1239, 1243, C IV $\lambda\lambda$1548, 1551, O III] $\lambda\lambda$1661, 1666, N II] $\lambda\lambda$2139, 2143, and Mg II $\lambda\lambda$2796, 2803 with Gaussians constrained to have fixed doublet separations, identical widths, and line ratios dictated by their oscillator strengths. At the resolution of the G140L grating setting, the Si IV λ1403

emission of the Si IV $\lambda\lambda$1394, 1403 doublet is blended with the O IV] λ1400 multiplets. We fit the combined Si IV and O IV] feature with multiple Gaussians, requiring the Si IV doublet to meet the same constraints as the other close doublets.

The observed fluxes of a few UV lines, such as Si IV $\lambda\lambda$1394, 1403 and C IV $\lambda\lambda$1548, 1551, were reduced by interstellar line absorption. We describe our procedure for correcting for this absorption in § 3.3.

3. DATA

3.1. *Optical Emission Line Fluxes*

Table 2 lists the measured spot 1 optical emission line fluxes, including previously published results from the 1998 March 7 (day 4030) data by Michael et al. (2000) and 1 σ upper flux limits for the [O II] $\lambda\lambda$3726, 3729 and [N I] $\lambda\lambda$5198, 5200 doublets. The 1 σ errors tabulated are only statistical errors. Systematic effects, such as fringing for the G750L data toward the near-IR region ($\lambda > 8500$ Å; Leitherer et al. 2000), might contribute additional uncertainties to the measured fluxes.

The tabulated fluxes have been dereddened with $E(B-V)$ of 0.16 (Fitzpatrick & Walborn 1990) and the extinction law of Cardelli, Clayton, & Mathis (1989) with an assumed R_V of 3.1. In the optical band the differences between the LMC extinction law and the Galactic law are negligible at low color excess (Fitzpatrick 1999). The interstellar extinction correction applied is listed in the last column of Table 2.

Spot 1 was observed in many neutral and lowly ionized species in the optical wavelengths. We did not detect any coronal lines such as [Fe X] λ6375. Most of the line fluxes increased with time at a rate comparable to that measured from WFPC2 photometry (Garnavich et al. 2001). At the low spectral resolution of both the G430L and G750L observing modes ($R = \lambda/\Delta\lambda = 530$–1040), definitive line identification remained a problem, especially for the [Fe II] emission lines. The Fe line identifications in Table 2 are based upon the modeling of the spot 1 Fe lines in C. S. J. Pun et al. (2002, in preparation). Moreover, several lines were blended. Table 2 lists possible contributing species and, in the case of [Fe II] lines, different multiplets. In contrast, line blending is not a problem in the medium-resolution G750M ($R \approx 6000$) data.

Fluxes in [O I] $\lambda\lambda$6300, 6363 and He I λ6678 were measured with the low-resolution G750L and medium-resolution G750M gratings in 1999 September within 17 days of each other. The two measurements agreed within uncertainties for the [O I] doublet. The two results differed by $\sim$50% for the low signal-to-noise ratio He I λ6678 data but were also within the noise level. This difference is probably a good indication of the detection limits of such faint lines.

3.2. *Optical Emission Line Widths*

For the medium-resolution G750M observations, apart from the line fluxes, we were also able to measure the peak emission velocities (V_0) and the widths ($V_{\rm FWHM}$) of the emission lines from the profile fits. Table 3 lists the results. The peak emission velocity measurements have been adjusted for the SN 1987A heliocentric velocity of 286 km s^{-1} (Wampler, Richichi, & Baade 1989). The 1998 March 0.″2 G750M results have also been adjusted for the off-center position of spot 1 within the aperture (see § 2). The main uncertainties in the measurements of both V_0 and $V_{\rm FWHM}$ are due to the contributions by emission from the stationary circumstellar ring, which dominated the emission by spot 1 near zero velocity for many species (see Fig. 4). The errors due to this contribution are generally smaller for the 1999 August 0.″1 observations than for the 1998 March 0.″2 ones.

For all emission lines, the line centroids from spot 1 were blueshifted, with peak velocity V_0 lying within the range -40 to -10 km s^{-1}. This result is consistent with the overall physical picture in which spot 1 is located on the near side of the equatorial ring (Sonneborn et al. 1998) and the shock entering spot 1 is moving toward the observer. We found no evidence that the peak velocity V_0 of spot 1 varied with time.

Most emission lines had widths (FWHM) within the range $\sim$150–180 km s^{-1}, except [N II] λ6583 and Hα, which had a slightly greater width, $V_{\rm FWHM} \gtrsim 200$ km s^{-1}. We detected no measurable change with time of the line widths except for Hα and [N II] λ6548. For Hα, the emission profile from the second observation in 1999 August could no longer be fitted well by a single Gaussian (to be discussed further in § 5.3). The width of the [N II] λ6548 emission, measured in 1999 August, was 1.5 times greater than that measured in 1998. However, we are inclined to attribute this increase to systematic error, since we detected no such increase in the other [N II] component at 6583 Å, where the line fluxes were $\sim$3 times stronger.

3.3. *UV Emission Lines*

3.3.1. *Interstellar Line Absorption*

Near the time of outburst, interstellar absorption lines of the C II λ1335 multiplet, Si IV $\lambda\lambda$1394, 1403, C IV $\lambda\lambda$1548, 1551, and Mg II $\lambda\lambda$2796, 2803 were observed in the UV continuum of SN 1987A with *IUE* operating in the high-resolution ($\Delta V \approx 30$ km s^{-1}) echelle mode (Blades et al. 1988; Welty et al. 1999). For each line, the dominant absorption component was centered at 281 km s^{-1}, near the SN 1987A heliocentric velocity of 286 km s^{-1} (Wampler et al. 1989), and had an FWHM of $\sim$80 km s^{-1}. Therefore, narrow emission lines ($v_{\rm FWHM} \simeq 10$ km s^{-1}) from the inner circumstellar ring from these species are completely blocked by the interstellar absorption (Fransson et al. 1989), as demonstrated by the absence of Si IV and C IV emission lines from the ring in Figure 3*a*.

Emission lines from spot 1, with $V_{\rm FWHM} \approx 200$ km s^{-1}, are not totally blocked by these interstellar absorption lines, as correctly predicted by Luo et al. (1994). However, the line profiles are altered and the observed fluxes are reduced substantially. Therefore, we must correct the measured C II, Si IV, C IV, and Mg II emission line fluxes to account for this absorption. The appropriate correction factors depend on the profile shapes of both the spot 1 emission and the intervening absorption. To make this correction, we assumed that the UV emission lines from spot 1 had Gaussian profiles with the same parameters as the optical lines as measured in the medium-resolution optical data (§ 2.2). We then estimated the amount of flux reduction in the UV emission lines by multiplying the assumed Gaussian profiles by the absorption profiles seen in the *IUE* data. The corresponding flux correction factors for the various emission lines are shown in Figure 5*a*. The correction factor is greatest for the Mg II $\lambda\lambda$2796, 2803 doublet, where the interstellar absorption is almost completely saturated between -50 and 300 km s^{-1}.

TABLE 2

HST/STIS Dereddened Optical Emission Line Fluxes from Spot 1

Emission	Central Wavelength (Å)	1998 Mar 7 (day 4030.0) Flux ($\times 10^{-16}$ ergs cm^{-2} s^{-1})	1999 Feb 21 (day 4380.9) Flux ($\times 10^{-16}$ ergs cm^{-2} s^{-1})	1999 Sep 1[a] (day 4570.0) Flux ($\times 10^{-16}$ ergs cm^{-2} s^{-1})	1999 Sep 18 (day 4587.4) Flux ($\times 10^{-16}$ ergs cm^{-2} s^{-1})	Extinction Correction[b]
[Ne v]	3425.8	...	...	2.3 ± 1.6	...	2.09
[N i]	3466.5	...	...	7.2 ± 1.9	...	2.08
[O ii]	3726.0 + 3728.8	...	...	< 6.0	...	2.02
Hι	3770.6	...	...	1.2 ± 1.0	...	2.01
Hθ	3797.9	...	...	1.6 ± 1.2	...	2.00
Hη	3835.4	...	...	4.4 ± 1.3	...	2.00
[Ne iii]	3868.7	...	...	13.3 ± 2.7	...	1.99
He i + Hζ	3888.7 + 3889.1	...	...	18.0 ± 2.8	...	1.98
Ca ii + [Fe ii] (8F)	3933.7 + 3931.4 + 3932.7	...	...	4.6 ± 1.0	...	1.97
He i + Ca ii + [Ne iii]	3964.7 + 3968.5 + 3968.7	...	...	12.5 ± 2.6[c]	...	1.96
Hϵ	3970.1	...	...	12.5 ± 2.6[c]	...	1.96
He i	4026.2	...	...	2.3 ± 1.0	...	1.95
[S ii]	4068.6	...	...	21.8 ± 2.4	...	1.93
[S ii]	4076.4	...	...	10.5 ± 1.3	...	1.93
Hδ	4101.7	...	...	12.9 ± 1.8	...	1.92
[Fe ii]	4244.0	...	...	2.6 ± 0.8	...	1.88
Hγ	4340.5	...	...	24.9 ± 2.5	...	1.85
[Fe ii] (21F)	4358.4	...	...	4.9 ± 2.5[c]	...	1.84
[O iii]	4363.2	...	...	4.9 ± 2.5[c]	...	1.84
He i	4387.9	...	...	1.2 ± 0.5	...	1.84
[Fe ii] (6F)	4416.3	...	...	3.2 ± 0.7	...	1.82
[Fe ii] (7F + 6F)	4452.1 + 4458.0	...	...	2.0 ± 0.7	...	1.81
He i + [Fe ii] (6F)	4471.5 + 4470.3	...	...	4.6 ± 0.7	...	1.81
Mg i]	4571.1	...	...	4.1 ± 1.0	...	1.78
[Fe ii] (4F + 5F)	4664.5, 4665.7 + 4665.0	...	...	2.0 ± 0.8	...	1.75
He ii + [Fe ii] (5F)	4685.7 + 4687.6	...	...	4.0 ± 0.7	...	1.75
[Fe ii] (20F)	4814.6	...	...	1.7 ± 0.5	...	1.71
Hβ	4861.3	...	...	49.6 ± 2.7	...	1.70
[Fe ii] (3F + 4F)	4889.7	...	...	1.7 ± 0.7	...	1.70
[Fe ii] (20F)	4905.4	...	...	1.4 ± 0.5	...	1.69
He i	4921.9	...	...	0.6 ± 0.3	...	1.69
[O iii]	4958.9	...	...	7.7 ± 1.4	...	1.68
[O iii]	5006.8	...	...	24.4 ± 1.1	...	1.67
He i	5015.7	...	...	4.5 ± 0.7	...	1.67
[Fe ii] (18F + 19F)	5158.0 + 5158.8	...	...	4.6 ± 0.6	...	1.64
[N i]	5197.9 + 5200.3	...	...	< 0.8	...	1.63
[Fe ii] (19F + 18F)	5261.6 + 5268.9, 5273.4	...	...	4.8 ± 0.7	...	1.62
[Fe ii] (19F)	5333.7	...	...	1.0 ± 0.3	...	1.60
[Fe ii] (19F)	5376.5	...	0.6 ± 0.4	1.4 ± 0.3	0.6 ± 1.0	1.60
He ii + [Fe ii] (17F)	5411.5 + 5412.6	...	1.0 ± 0.3	1.5 ± 0.4	1.4 ± 0.6	1.59
[Fe ii] (34F)	5527.3	...	...	1.1 ± 0.3	1.4 ± 0.5	1.57
[O i]	5577.4	...	1.0 ± 0.5	1.9 ± 0.4	2.3 ± 0.6	1.57
[N ii]	5754.6	...	16.9 ± 2.0	...	20.8 ± 1.4	1.54
He i	5875.7	...	9.3 ± 2.1	...	14.4 ± 1.1	1.53
[O i]	6300.3	13.2 ± 1.0	18.7 ± 1.5	27.1 ± 1.2	25.9 ± 1.9	1.48
[S iii]	6312.1	...	...	...	0.6 ± 0.3	1.48
[O i]	6363.8	4.9 ± 0.6	7.4 ± 0.5	8.1 ± 0.9	8.0 ± 1.3	1.47
[N ii]	6548.1	8.2 ± 1.1	...	9.5 ± 1.0	...	1.45
Hα	6562.8	67.9 ± 1.8	...	179.8 ± 3.9	...	1.45
[N ii]	6583.5	19.0 ± 1.3	...	31.1 ± 1.7	...	1.45
He i	6678.2	1.2 ± 0.3	1.6 ± 0.2	2.2 ± 0.5	3.5 ± 0.6	1.44
[S ii]	6716.5	1.3 ± 1.3	...	1.3 ± 0.8	...	1.44
[S ii]	6730.8	1.3 ± 0.5	...	2.2 ± 0.7	...	1.44
He i	7065.2	...	4.3 ± 0.9	...	6.3 ± 0.7	1.40
[Ar iii]	7135.9	...	2.6 ± 0.4	...	2.5 ± 0.7	1.40
[Fe ii] (14F)	7155.2	...	3.0 ± 0.6	...	4.3 ± 0.8	1.39
[Fe ii] (14F)	7172.0	...	3.7 ± 0.7	...	1.2 ± 0.5	1.39
[Ca ii]	7291.5	...	4.1 ± 0.7	...	6.2 ± 0.9	1.38
[Ca ii] + [O ii]	7323.9 + 7320, 7330	...	20.9 ± 4.0	...	25.2 ± 1.3	1.38
[Ni ii] (2F)	7377.9	...	0.4 ± 0.5	...	2.1 ± 0.9[d]	1.37
[Fe ii] (14F)	7388.2	...	0.3 ± 0.4	...	2.1 ± 0.9[d]	1.37
[Ni ii] (2F)	7411.6	...	0.4 ± 0.4	...	Weak	1.37

TABLE 2—*Continued*

Emission	Central Wavelength (Å)	1998 Mar 7 (day 4030.0) Flux ($\times 10^{-16}$ ergs cm^{-2} s^{-1})	1999 Feb 21 (day 4380.9) Flux ($\times 10^{-16}$ ergs cm^{-2} s^{-1})	1999 Sep 1[a] (day 4570.0) Flux ($\times 10^{-16}$ ergs cm^{-2} s^{-1})	1999 Sep 18 (day 4587.4) Flux ($\times 10^{-16}$ ergs cm^{-2} s^{-1})	Extinction Correction[b]
[Fe II] (14F)	7452.6	...	0.4 ± 0.2	...	1.1 ± 0.5	1.36
[Fe II] (13F)	8617.0	...	1.1 ± 0.4	...	4.4 ± 0.9	1.27
[S III]	9068.6	...	0.8 ± 0.5	...	1.4 ± 0.9	1.24
[S III]	9530.6	...	4.8 ± 1.7	...	11.2 ± 1.6	1.22

[a] Combining the G750M data taken on 1999 August 30 (day 4568.0) and the G430L data taken on 1999 September 3 (day 4571.9).
[b] $E(B-V) = 0.16$, and the extinction correction law of Cardelli et al. 1989, with $R_V = 3.1$.
[c] Emission blended in the G430L data; separate component determined from 2000 January data (C. S. J. Pun et al. 2002, in preparation).
[d] Emissions blended in the G750L data.

The flux correction factor due to interstellar absorption is sensitive to the assumed widths ($V_{\rm FWHM}$) and peak (V_0) velocities of assumed line profiles from spot 1. Figure 5*b* illustrates this dependence for the important case of C IV $\lambda\lambda$1548, 1551. We see that the flux correction factor increases moderately with decreasing $V_{\rm FWHM}$ for $V_{\rm FWHM} > 200$ km s^{-1} but becomes very sensitive to both $V_{\rm FWHM}$ and V_0 for $V_{\rm FWHM} < 150$ km s^{-1}.

As we shall discuss in § 5.3, the peak velocities and widths of the emission lines from spot 1 depend on the detailed geometry and hydrodynamics of the shocks entering the spot, which are unknown. It is not obvious that the optical and UV emission lines should have the same peak velocities and widths. However, in the plane-parallel shock model that we describe in § 4, we found that the peak velocities of emission from spot 1 were almost identical in both the UV and optical wavelengths. Therefore, we used the measured peak spot 1 velocities from the medium-resolution optical observations, $V_0 = -30 \pm 15$ km s^{-1} (see Table 3), to estimate the flux correction factors to account for interstellar absorption of the UV emission lines.

3.3.2. *Widths of the UV Emission Lines*

The far-UV emission lines from spot 1 are poorly resolved at the spectral resolution of the G140L grating ($\Delta V \approx 250$ km s^{-1} at 1500 Å). For these lines, we attempted to establish the relation between the actual and observed widths through Monte Carlo simulations. For the simulations, we assumed that the intrinsic spot 1 emission lines had (1) a Gaussian shape with FWHM as a variable parameter, (2) emission peaked at -30 km s^{-1}, and (3) a flux ratio of the doublets dictated by their oscillator strengths.

The dotted line in Figure 6*a* shows a model C IV $\lambda\lambda$1548, 1551 profile, assuming $V_{\rm FWHM} = 150$ km s^{-1} and line flux ratio $I(\lambda 1548)/I(\lambda 1551) = 21$. The solid line shows a subsection of the high-resolution *IUE* spectrum with the absorption-line profile for the C IV doublet. For each input FWHM, we multiplied the model input emission line by the measured *IUE* absorption spectrum. Figure 6*b* shows a typical result. We convolved this profile with the line-spread function (LSF) of the detector for the slit aperture of the data set. The LSF for each emission line was interpolated from the measured LSFs at 1200, 1500, and 1600 Å. The LSF typically has a narrow peak ($\sim$1.5 pixels) and a broad wing that extends to $\sim$10 pixels on either side of the peak (Leitherer et al. 2000). Figure 6*c* shows a typical example of the LSF for the G140L grating at 1550 Å with the 0.″2 aperture.

For each emission line, we normalized the resulting convolved profile to the photon counts for each observation. The thick solid line in Figure 6*d* shows the normalized model C IV line profile for the 1999 October observation. We constructed a simulated observed profile (the thin solid line in Fig. 6*d*) by applying random noise to the model profile and sampling it at the spectral resolution of the G140L grating. Finally, we fitted the simulated profile with Gaussians in the same way as the real data. The dotted line in Figure 6*d* shows such a fit.

For each input model FWHM velocity, we ran 10,000 simulations and generated an array of the corresponding observed line widths. Figure 7 shows the median and the 68.3% (1 σ) upper and lower limits of the array plotted

TABLE 3
PEAK EMISSION VELOCITY AND FWHM WIDTH OF SPOT 1 EMISSIONS

	1998 MAR 7 (DAY 4030.0)		1999 AUG 30 (DAY 4568.0)	
EMISSION LINE	Width	Peak Velocity (km s^{-1})	Width	Peak Velocity (km s^{-1})
[O I] λ6300	154 ± 7	-13 ± 18	172 ± 5	-34 ± 5
[O I] λ6363	179 ± 14	-27 ± 20	182 ± 11	...
[N II] λ6548	165 ± 11	-37 ± 24	230 ± 16	-11 ± 4
Hα λ6563	253 ± 4	-29 ± 3	225 ± 3	-35 ± 2
[N II] λ6584	204 ± 7	-17 ± 10	215 ± 7	-19 ± 2
He I λ6678	177 ± 38	...	183 ± 27	...
[S II] λ6717	113 ± 40	...	84 ± 24	...
[S II] λ6731	149 ± 48	...	134 ± 20	...

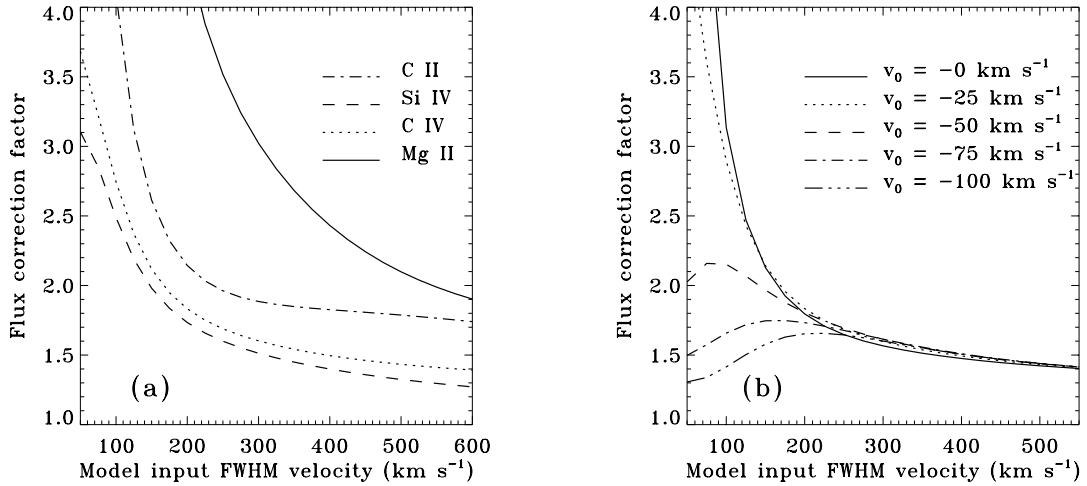

FIG. 5.—(*a*) Interstellar absorption correction factors for emission lines C II λλ1335, 1336 (*dot-dashed line*), Si IV λλ1394, 1403 (*dashed line*), C IV λλ1548, 1551 (*dotted line*), and Mg II λλ2796, 2803 (*solid line*). The peak velocity V_0 of the model spot 1 emission is assumed to be −30 km s^{-1}. (*b*) Correction factor for the C IV λλ1548, 1551 doublet is plotted against the FWHM velocity of the input model spot 1 Gaussian profile with peak velocities $V_0 = 0$ (*solid line*), −25 (*dotted line*), −50 (*dashed line*), −75 (*dot-dashed line*), and −100 km s^{-1} (*triple-dot–dashed line*).

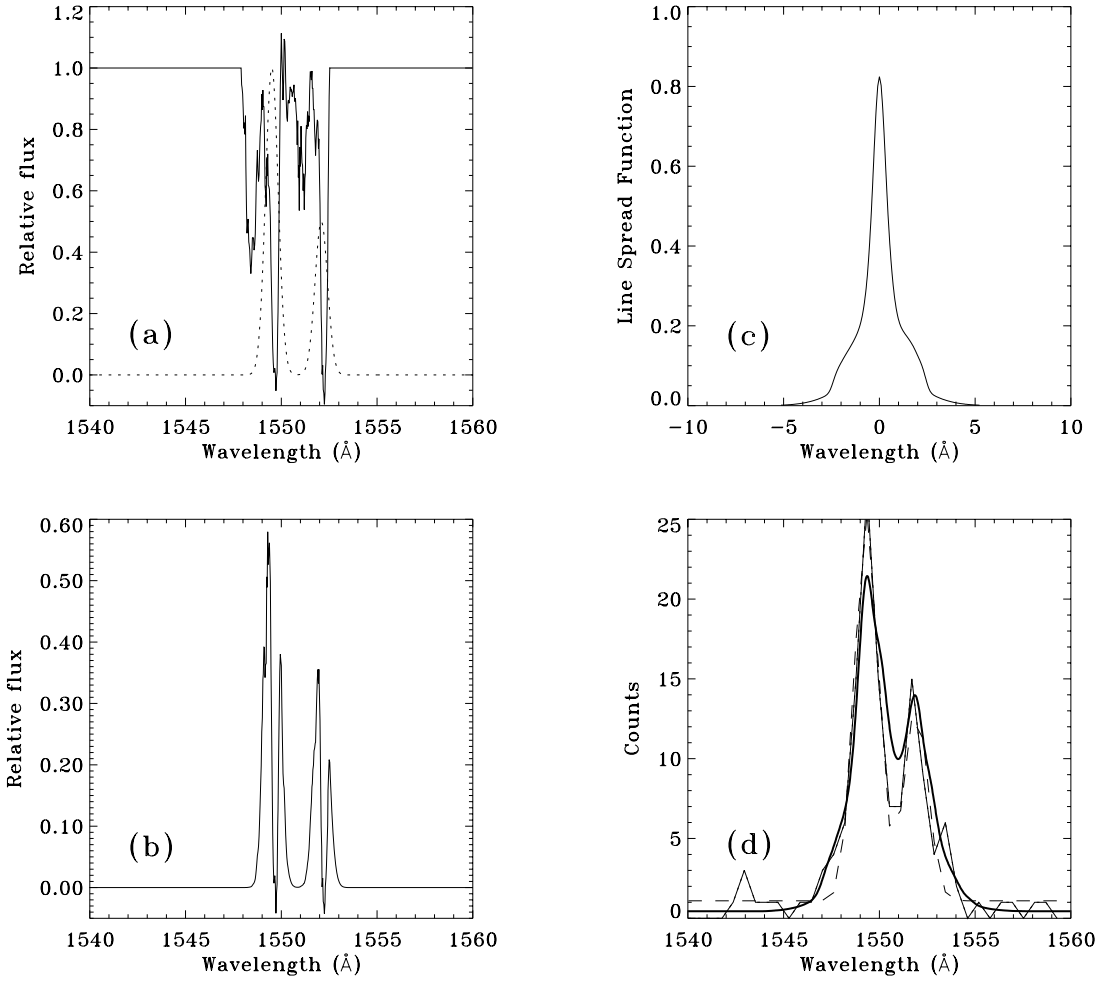

FIG. 6.—(*a*) *IUE* high-dispersion spectrum of the C IV λλ1548, 1551 absorption lines (*solid line*), overlayed with a model Gaussian spot 1 line profile of the C IV emission line (*dotted line*). The FWHM width of the model profile is 150 km s^{-1}, and it peaks at −30 km s^{-1} with line ratio $I(\lambda1548)/I(\lambda1551) = 21$. (*b*) Model C IV spot 1 spectrum after the interstellar line absorption. (*c*) LSF of STIS/MAMA G140L grating for the 0″.2 aperture at 1500 Å. (*d*) Model "observed" spectrum after convolving the model profile after absorption with the LSF (*thick solid line*). Example of a Monte Carlo generated line profile of the C IV doublet, normalized to the integrated counts of the 1999 October data, is also shown (*thin solid line*), along with the best-fit double-Gaussian function to this profile (*dashed line*). In this example, the best-fit $V_{\rm FWHM} = 281$ km s^{-1}.

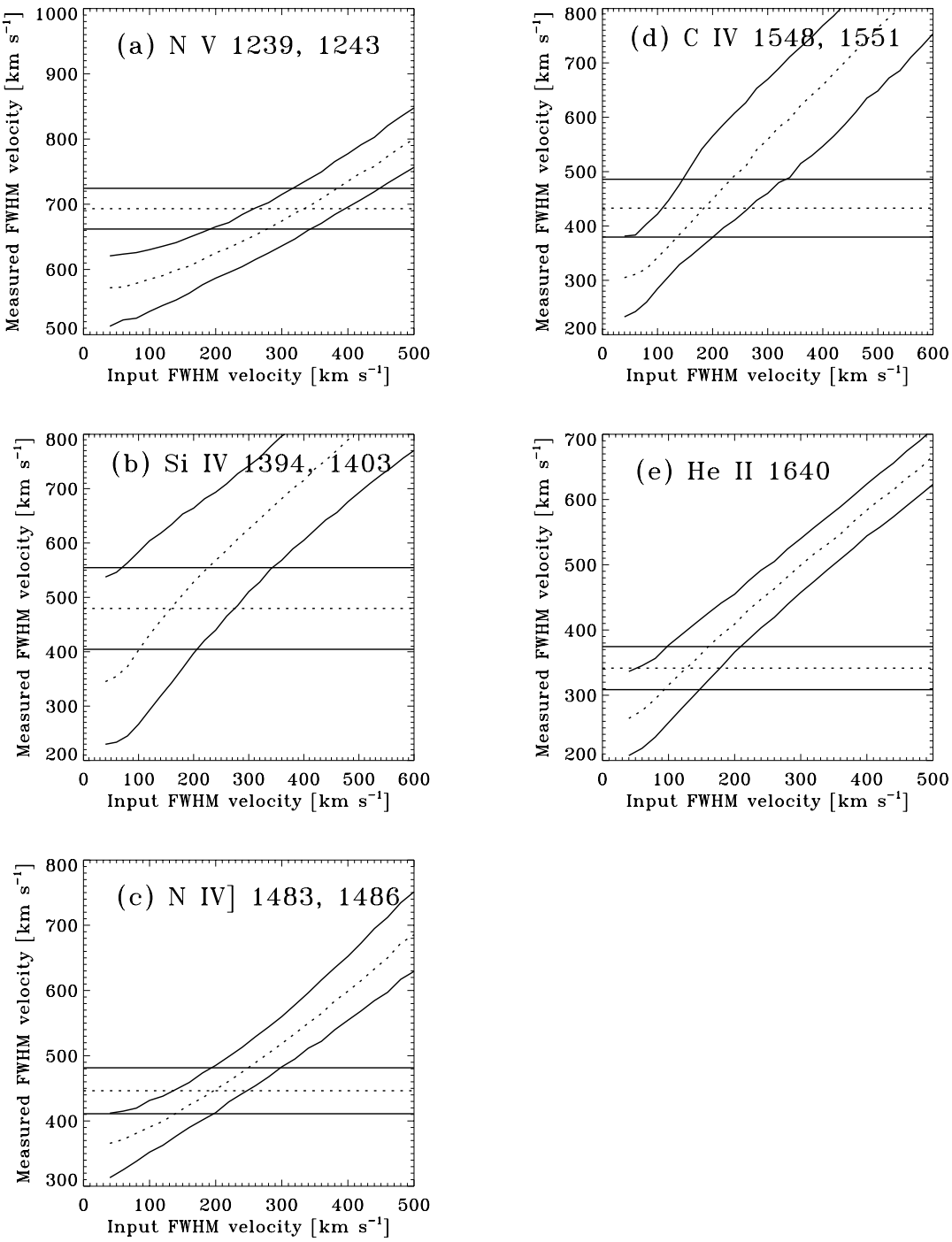

FIG. 7.—Monte Carlo results of the relation between the intrinsic spot 1 emission width and the measured widths from Gaussian fittings for the 1999 October G140L 0.″2 observations in (*a*) N V λλ1239, 1243; (*b*) Si IV λλ1394, 1403; (*c*) N IV] λλ1483, 1486; (*d*) C IV λλ1548, 1551; and (*e*) He II λ1640.

against the model input widths of the various observed emission lines. We use these results to convert the observed line widths from the STIS data, shown as horizontal lines in Figure 7, to the intrinsic widths of the lines emitted by spot 1. We did not attempt to model the near-UV G230L data in this way because the spectral resolution for this grating setting ($\Delta V \approx 450$ km s^{-1} at 2500 Å) was too low for such a procedure to yield useful results.

For all emission lines except the N V doublet, we found a 1 σ upper limit of FWHM $\lesssim$ 300 km s^{-1}, consistent with the measurements from the medium-resolution optical data. The lower limit to the assumed FWHM is important because the flux correction factors for all UV emission lines are sensitive to the input line widths for FWHM $<$ 150 km s^{-1}. We took this lower limit to be the same as the measured lower limit for the optical lines, that is, FWHM $>$ 100 km s^{-1}.

3.3.3. *UV Line Fluxes and Line Widths*

Table 4 lists the fluxes of UV lines from spot 1 inferred from the Gaussian line fits (corrected for extinction) and the

TABLE 4

HST/STIS Dereddened UV Emission Line Fluxes and Line Widths of Spot 1

Emission	Central Wavelength[a] (Å)	Flux Correction[b]	1997 Sep 27 (day 3869.3)		1999 Feb 27 (day 4387.6)		1999 Sep 27 (day 4596.2)		Extinction Correction[c]
			Flux ($\times 10^{-16}$ ergs cm^{-2} s^{-1})	Width (km s^{-1})	Flux ($\times 10^{-16}$ ergs cm^{-2} s^{-1})	Width (km s^{-1})	Flux ($\times 10^{-16}$ ergs cm^{-2} s^{-1})	Width (km s^{-1})	
N v.....	1238.8 + 1242.8	...	15.0 ± 5.3	$270^{+220}_{-...}$	51.5 ± 6.4	380^{+150}_{-180}	79.6 ± 5.6	330^{+110}_{-140}	5.93
C ii.....	1335 multiplet	$2.6^{+1.5}_{-0.8}$	...	...	...	...	$7.3^{+5.4}_{-4.2}$	...	4.96
Si iv.....	1393.8 + 1402.8	$2.0^{+0.8}_{-0.5}$	$5.8^{+3.2}_{-2.6}$	...	$14.9^{+6.9}_{-5.1}$	$130^{+150}_{-...}$	$21.0^{+10.9}_{-8.8}$	$160^{+180}_{-...}$	4.57
O iv].....	1400 multiplet	...	6.1 ± 1.7	...	11.0 ± 2.4	...	11.1 ± 2.9	...	4.53
N iv].....	1483.3	...	5.9 ± 1.5	...	6.5 ± 1.3	$110^{+130}_{-...}$	9.2 ± 1.4	$200^{+100}_{-...}$	4.16
N iv].....	1486.5	...	6.1 ± 1.5	...	11.5 ± 1.9	$110^{+130}_{-...}$	14.2 ± 1.8	$200^{+100}_{-...}$	4.15
C iv	1548.2 + 1550.8	$2.1^{+1.0}_{-0.5}$	$24.1^{+13.3}_{-9.0}$	...	$37.3^{+18.9}_{-11.5}$	$150^{+100}_{-...}$	$45.7^{+23.4}_{-14.4}$	$180^{+150}_{-...}$	3.95
[Ne iv]	1601.5 + 1601.7	...	...	...	...	...	3.9 ± 2.4	...	3.81
He ii	1640.4	...	13.1 ± 3.4	...	36.7 ± 4.8	$100^{+80}_{-...}$	64.3 ± 8.9	$130^{+80}_{-...}$	3.73
O iii	1660.8 + 1666.2	...	...	...	...	...	13.7 ± 2.8	...	3.69
C iii]	1908.7	...	...	...	...	...	19.7 ± 5.2	...	3.56
N ii].....	2139.0 + 2142.8	...	...	...	...	...	18.5 ± 3.2	...	4.02
C ii	2325 multiplet	...	...	...	...	...	33.4 ± 2.2	...	3.43
Si ii.....	2334.6	...	...	...	...	...	6.9 ± 1.5	...	3.39
[O ii].....	2470.3	...	...	...	...	...	10.7 ± 1.5	...	2.93
	2736.7[d]	...	...	...	...	...	2.3 ± 0.8	...	2.51
	2746.3[d]	...	...	...	...	...	3.0 ± 0.8	...	2.50
Mg ii	2795.5 + 2802.7	$6.6^{+14.2}_{-3.9}$	...	...	...	...	230^{+493}_{-135}	...	2.45

[a] Wavelength in λ_{vac} for $\lambda < 2000$ Å, λ_{air} for $\lambda > 2000$ Å.

[b] Corrected for LMC line absorption assuming spot 1 FWHM velocity $V_{FWHM} = 150^{+150}_{-50}$ km s^{-1} and peak velocity $V_0 = -30 \pm 15$ km s^{-1}.

[c] $E(B-V)_{LMC} = 0.06$ and $E(B-V)_{Galactic} = 0.10$ are assumed, along with $R_V = 3.1$. For the LMC component, the 30 Doradus extinction function of Fitzpatrick 1986 is used; for the Galactic component, the Seaton 1979 correction law is used.

[d] Uncertain identification; refer to text.

intrinsic line widths derived from the Monte Carlo simulations. The tabulated fluxes for the C II, Si IV, C IV, and Mg II doublet have been corrected for interstellar line absorption assuming an intrinsic spot 1 line width $V_{\rm FWHM} = 150^{+150}_{-50}$ km s^{-1} with peak emission at $V_0 = -30 \pm 15$ km s^{-1}. The flux correction factors applied for these lines are also listed in Table 4. We also corrected the fluxes for interstellar extinction by assuming $E(B-V)_{\rm LMC} = 0.06$, $E(B-V)_{\rm Galactic} = 0.10$, and $R_V = 3.1$. At UV wavelengths, the choice of extinction function is important because the correction is substantial and is known to vary from place to place (see Pun et al. 1995 for a discussion on UV extinction correction for SN 1987A). We used the 30 Doradus extinction function of Fitzpatrick (1986) for the LMC component and the Seaton (1979) function for the Galactic component.

The far-UV G140L data had slightly higher kinematic resolution ($\Delta V \approx 250$ km s^{-1}) than the low-resolution optical G430L and G750L data. However, the individual components of the C II λ1335 and O IV] λ1400 multiplets remained unresolved in the data. There were more uncertainties with line identifications in the lower resolution ($\Delta V \approx 300$–650 km s^{-1}) near-UV G230L data, such as the unidentified emission features near 2737 and 2746 Å. On the other hand, we identified emission features near 2324 and 2334 Å as the C II λ2325 multiplet and Si II λ2335, respectively. We ruled out the alternative identification of [O III] $\lambda\lambda$2322, 2332 because the observed line ratios, $I(\lambda2324)/I(\lambda2334) \approx 5$ and $I(\lambda2324)/I(\lambda4363) \approx 7$, were much different from the theoretical [O III] line ratios of $\sim$280 and 0.12, respectively. These [O III] line ratios are determined only by the atomic transition probabilities and are independent of the excitation model.

The fluxes of all far-UV lines from spot 1 increased with time during the three observations taken from 1997 September (day 3869) to 1999 October (day 4606). The rate of increase differed for features from different ions, ranging from $I(\text{day } 3869)/I(\text{day } 4596) = 5.3$ for N V λ1240 to 1.9 for C IV λ1550. We will discuss the time dependence of the UV emission line fluxes in § 5.2.

4. INTERPRETATION

4.1. *Impact Hydrodynamics*

In our working model for spot 1, we assume that the UV and optical emission lines observed are caused by radiative shocks that develop where the supernova blast wave strikes dense gas protruding inward from the circumstellar ring. As we shall show, the spectrum and profiles of the emission lines from such shocks are sensitive to the density distribution and geometry of this protrusion, which are probably quite complex and cannot be resolved even with the *HST*. Our approach here therefore is to illustrate the salient physics of the spectrum formation with a few idealized "toy models," which we believe will guide us toward a better understanding of the properties of a more realistic model.

Following the previous work of Luo et al. (1994) and Borkowski et al. (1997b), we show in Figure 8 hydrodynamic simulations for two models of a fast shock overtaking a dense gas cloud. In each model, we assume that a fast plane-parallel blast wave traveling through a uniform medium of relatively low density overtakes a cloud of substantially greater uniform density. The cloud boundary is approximated as a density discontinuity. In each simulation, the blast wave drives a transmitted shock into the cloud, while a reflected shock travels backward toward the interior of the remnant. As the blast wave overtakes the obstacle, the surface area of the transmitted shock increases. The transmitted shock propagates with a range of velocities depending on shape and density of the obstacle.

The simulations are calculated using the hydrodynamic code VH-1 (Strickland & Blondin 1995), which is based on the piecewise parabolic method of Colella & Woodward (1984). Radiative cooling is included in the code using an operator splitting technique. We have used a nonequilibrium ionization cooling curve calculated with the plane-parallel shock code described in § 4.2 with abundances typical of the equatorial ring. At the resolution of the simulations, we are not always able to resolve the cooling timescale of the shocks. However, this computational limitation does not seriously affect the behavior of the overall hydrodynamics of the interaction. Moreover, we have modeled the blast wave as a single planar shock rather than using the full double-shock structure present in the remnant. We will comment on the effects of ignoring the full double-shock structure in § 6.

The two scenarios depicted in Figure 8 show two different behaviors for the development of radiative shocks in the obstacle. The important parameter distinguishing their behavior is $t_{\rm cool}/t_{\rm cross}$, where $t_{\rm cool}$ is the typical cooling time for the transmitted shocks and $t_{\rm cross}$ is the time it takes for the fast shock to cross the obstacle. As we will discuss in § 5.2.2, the interpretation of the observed light curves of lines emitted from the shocks depends on which behavior is dominant in spot 1.

The simulation in the left panels of Figure 8 (scenario 1) is one in which $t_{\rm cool}$ is comparable to $t_{\rm cross}$, so that not all of the shocks have become radiative. For this simulation we assume that the obstacle is a spherical cloud of density $\rho_0 = 10^4$ amu cm^{-3} and diameter $d_{\rm spot} = 4 \times 10^{16}$ cm. This geometry allows the shock to be driven into the back side of the obstacle. Even after the blast wave has completely overtaken the obstacle, the shocks transmitted into the front end of the obstacle have not yet undergone thermal collapse and are nonradiative (NR) because of the high impact velocity. On the other hand, the shocks transmitted into the sides and back of the obstacle have lower velocities owing to the oblique incidence of the blast wave. The shocked gas behind these parts of the transmitted shock has a lower temperature and a shorter radiative cooling time. A dense layer of cooled gas (R) is developed as a consequence (to be discussed further in § 5.2).

Scenario 2 in Figure 8 represents an example in which the cooling time for the transmitted shock is much shorter than the timescale for the blast wave to cross the cloud $t_{\rm cool} \ll t_{\rm cross}$, regardless of incidence angle of the blast wave. We assume that the obstacle is an elongated protrusion with a higher density, $\rho_0 = 10^5$ amu cm^{-3}. With the high density of the obstacle, all the transmitted shocks undergo thermal collapse soon after impact.

We recognize that these idealized models in Figure 8 do not represent the true shape and density distribution of the obstacle. However, given the limited observations at hand, we believe it is more fruitful to explore how well we can fit the data with a few idealized models or combinations thereof than to explore fits of more complicated hydrodynamic models (see § 6).

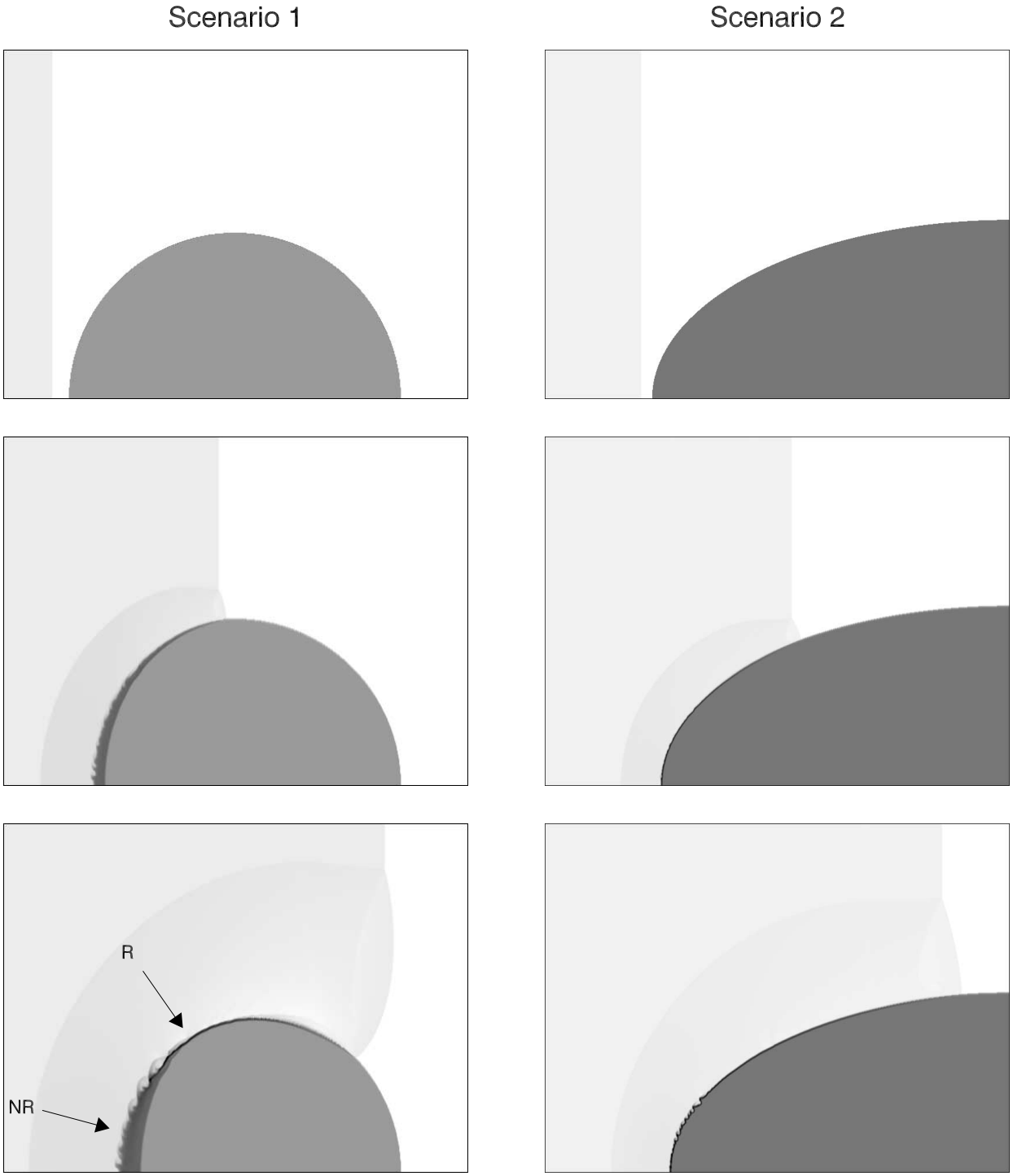

FIG. 8.—Two-dimensional cylindrically symmetric hydrodynamical simulations (800 × 600 zones) of a blast wave overtaking a dense obstacle with darker shade representing higher density. The left panels (scenario 1) show the development of a shock ($V_b = 2000$ km s^{-1}, $\rho_{\rm H\ II} = 150$ amu cm^{-3}, $d_{\rm spot} = 4 \times 10^{16}$ cm, $\rho_0 = 10^4$ amu cm^{-3}) where the cooling time is comparable to the time for the fast shock to cross the obstacle, i.e., $t_{\rm cool} \approx t_{\rm cross}$. Shocks that have undergone radiative collapse and developed dense postshock layers (R) and shock that remained nonradiative (NR) are indicated. The right panels (scenario 2) show the development of a shock ($V_b = 3500$ km s^{-1}, $\rho_{\rm H\ II} = 150$ amu cm^{-3}, $d_{\rm spot} \approx 4 \times 10^{16}$ cm, $\rho_0 = 10^5$ amu cm^{-3}) where $t_{\rm cool} \ll t_{\rm cross}$. As a result of the high density in this obstacle, all of the transmitted shocks undergo thermal collapse almost immediately.

4.1.1. *Transmitted Shock Velocities*

The driving pressure P_b behind a hypersonic blast wave propagating with velocity V_b through a medium of density ρ is given by $P_b = \frac{3}{4}\rho V_b^2$. Immediately after the blast wave passes the surface of an obstacle, a transmitted shock propagates into the obstacle with velocity

$$V_s = \left(\frac{P_s}{\rho_0}\right)^{1/2},$$

where P_s is the pressure at the surface of the obstacle and ρ_0

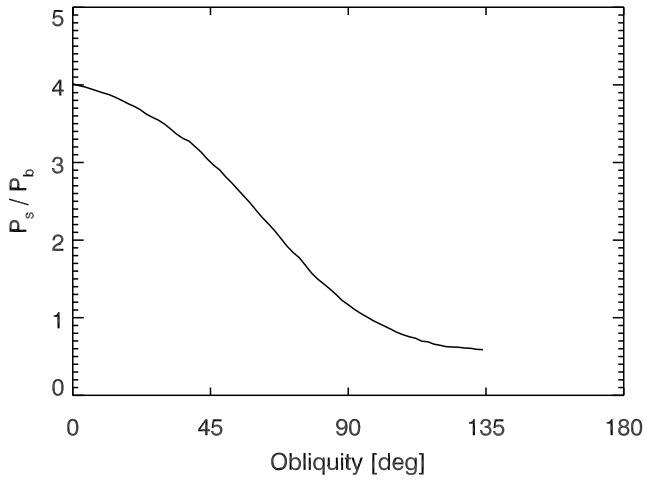

FIG. 9.—Pressure behind the reflected shock as a function of obliquity immediately after impact of the blast wave for a spherical cloud having a density enhancement $\delta = \rho_0/\rho_{\rm H\ II} \approx 70$. We do not show the function for obliquities higher than 135° since the behavior at the back of a cloud is complex and highly time dependent as a result of the "healing" of the blast wave.

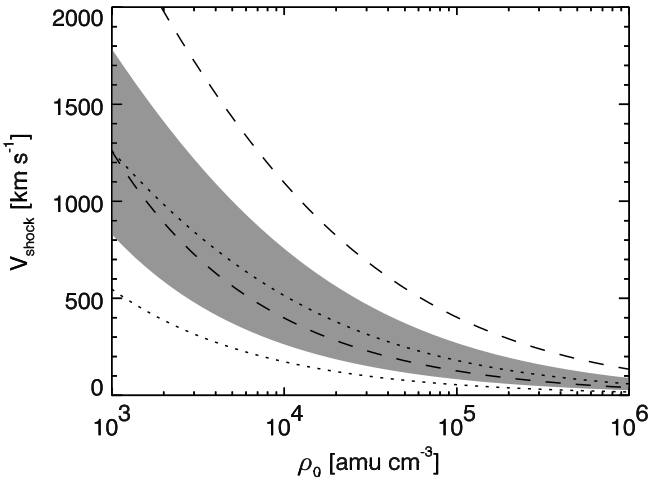

FIG. 10.—Range of transmitted shock velocities ($V_{\rm shock}$) as a function of preshock density (ρ_0) for three different estimates of the blast-wave pressure. The shaded gray region shows the range of transmitted shock velocities (due to obliquity) for our best estimate of the blast-wave pressure ($V_b = 3500$ km s^{-1}, $\rho_{\rm H\ II} = 150$ amu cm^{-3}). The upper boundary is the velocity of the transmitted shock at the tip of the protrusion, and the lower boundary is the velocity at the side of the protrusion. The range of allowed shock velocities for our high blast-wave pressure estimate ($V_b = 4100$ km s^{-1}, $\rho_{\rm H\ II} = 250$ amu cm^{-3}; *dashed line*) and the low estimate ($V_b = 2800$ km s^{-1}, $\rho_{\rm H\ II} = 100$ amu cm^{-3}; *dotted line*) is also shown.

is the preshock density of the obstacle. The value of P_s at a given location on the cloud surface rises sharply as the blast wave first strikes it, then decreases as the reflected shock propagates away from it. Over a timescale comparable to that for the blast wave to overtake the obstacle, P_s decreases by a factor of ~1.5–2 (Borkowski et al. 1997b). Immediately after the passage of the blast wave, the ratio P_s/P_b at any given point on the cloud surface depends on two parameters: (1) the obliquity angle θ between the direction of the blast and the inward normal to the surface of obstacle and (2) the preshock density ratio $\delta = \rho_0/\rho_{\rm H\ II}$ between the obstacle and the ambient H II region. Figure 9 illustrates the dependence on obliquity for a blast wave with a density contrast $\delta \approx 70$ impacting on a spherical cloud. At the point of first contact, i.e., $\theta = 0$, the driving pressure is at its maximum value and $P_s/P_b \approx 4$. As the obliquity of the impact increases, the driving pressure decreases. With a factor of ~10 decrease in pressure due to obliquity, the initial velocity of the transmitted shock on the edges of the protrusion is only ~30% of that at the tip of the protrusion.

We estimate the pressure behind the blast wave P_b from the relation $P_b = \frac{3}{4}\rho V_b^2$. By fitting the radio remnant of SN 1987A from year 1992 to 1995 with a shell model, Gaensler et al. (1997) measured the velocity of the blast wave to be $V_b = 2800 \pm 400$ km s^{-1}. Using more recent radio observations, Manchester et al. (2002) updated the value of V_b to be 3500 ± 100 km s^{-1}. However, they also noticed that in data taken since approximately 1998, the radio remnant can no longer be fitted well with the simple shell model but instead with a combined shell and multiple point sources model. Manchester et al. (2002) estimated that this leads to a 30% uncertainty in the measured expansion velocity. On the other hand, by modeling the observed X-ray emission from the blast wave before any spots appeared on the circumstellar ring, Borkowski et al. (1997b) found a slightly higher velocity for the blast wave, $\langle V_b \rangle = 4100$ km s^{-1}, and a density of the H II region inside the ring, $\rho_{\rm H\ II} = 150$ amu cm^{-3}. These results are consistent with the estimates of Chevalier & Dwarkadas (1995) and the upper limit $\rho_{\rm H\ II} < 240$ amu cm^{-3} determined by Lundqvist (1999). We estimate the blast-wave pressure to be within the range $P_b = (1\text{–}5) \times 10^{-5}$ dynes cm^{-2}.

The preshock density ρ_0 of the obstacle is even more uncertain. The density of the ring has been determined from the rate of fading of the optical and UV emission lines (Lundqvist & Fransson 1996; Sonneborn et al. 1997). At the time of emission maximum (approximately day 350), the radiation was dominated by gas of relatively high density, $\rho_0 \sim 5 \times 10^4$ amu cm^{-3}. However, the emission from the higher density gas faded rapidly, and the emission at later times was dominated by gas of lower density, $\rho_0 \sim 10^4$ amu cm^{-3} (Maran et al. 2000). The gas in spot 1 might have even higher density than the value derived from optical and UV lines. The fact that spot 1 lies inside the inner circumstellar ring might be due to the fact that it resisted ablation from the ionizing radiation and stellar wind of the progenitor as a result of its enhanced density.

We summarize the possible range of transmitted shock velocities in Figure 10. The shaded gray region shows the range of transmitted shock velocity V_s as a function of the preshock density of the obstacle ρ_0 for our best estimate of the blast-wave pressure ($V_b = 3500$ km s^{-1}, $\rho_{\rm H\ II} = 150$ amu cm^{-3}). The upper boundary is the velocity of the transmitted shock at the tip of the protrusion, and the lower boundary is the velocity at the side. We also show in Figure 10 the corresponding shock velocity range for our high estimate of the blast-wave pressure ($V_b = 4100$ km s^{-1}, $\rho_{\rm H\ II} = 250$ amu cm^{-3}; *dashed line*) and our low-pressure estimate ($V_b = 2800$ km s^{-1}, $\rho_{\rm H\ II} = 100$ amu cm^{-3}; *dotted line*). Assuming a preshock obstacle density of $(1\text{–}5) \times 10^4$ amu cm^{-3}, it is apparent that a range of shock velocities (~100–1000 km s^{-1}) can be present in the obstacle.

4.2. *Shock Structure*

In this section we review the relevant physics of shock fronts that we need to interpret the emission-line spectrum of spot 1. We use the 1991 version of the Raymond shock code (Cox & Raymond 1985) for illustration. The code calculates the nonequilibrium ionization and excitation of the postshock flow in a one-dimensional steady state shock for any given input parameters such as shock velocity and preshock densities. For any specified electron (T_e) and ion (T_i) temperatures at the shock front, the code calculates their equilibration through Coulomb collisions. We assume a ratio of $T_e/T_i = 0.2$ for our models. The code calculates the upstream equilibrium preionization and the downstream photoionization of the gas and derives the postshock density, temperature, and ionization structure in the gas. The code also calculates the local emissivity throughout the shock and the integrated fluxes over the entire column behind the shock front, including continuum and line emission from both allowed and forbidden transitions of H, He, C, N, O, Ne, Mg, Si, S, Ar, Ca, Fe, and Ni.

We adopted the LMC abundances measured by Russell & Dopita (1992) in all elements except for He, C, N, and O, where the ring abundances derived by Lundqvist & Fransson (1996) are used instead. The other exception is Si, where the abundance of Welty et al. (1999) is used because of the large uncertainty in the measurements by Russell & Dopita (1992). We call this set of values the "ring" abundance (H : He : C : N : O : Ne : Mg : Si : S : Ar : Ca : Fe : Ni := $1 : 0.25 : 3.24 \times 10^{-5} : 1.82 \times 10^{-4} : 1.58 \times 10^{-4} : 4.07 \times 10^{-5} : 2.95 \times 10^{-5} : 2.51 \times 10^{-5} : 5.01 \times 10^{-6} : 1.95 \times 10^{-6} : 7.76 \times 10^{-7} : 1.70 \times 10^{-5} : 1.10 \times 10^{-6}$).

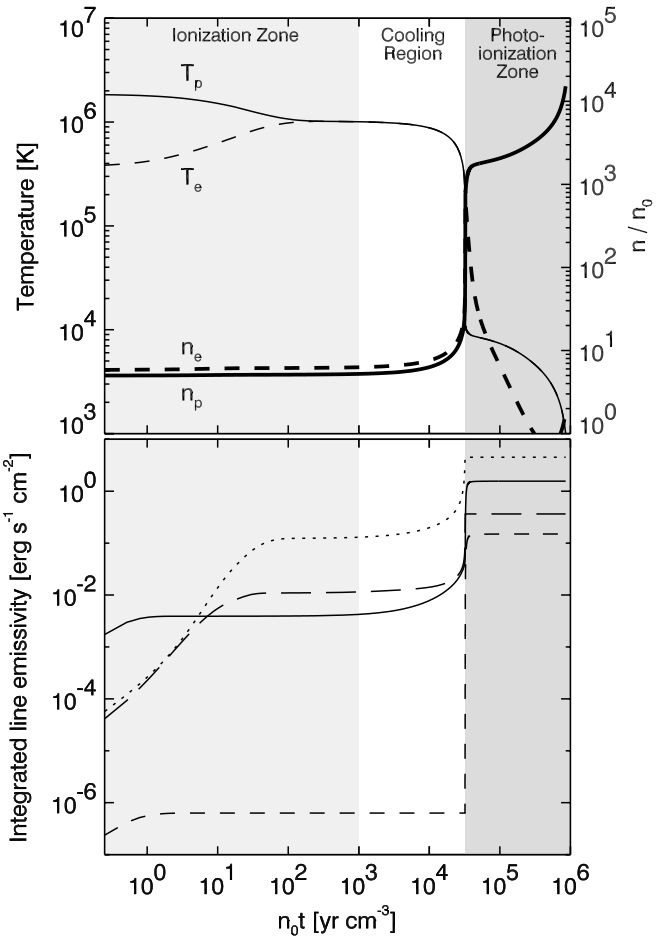

FIG. 11.—*Top:* Temperature (*thin line*) and density (*thick line*) structure for electrons (*dashed line*) and protons (*solid line*) in a radiative shock of velocity $V_s = 250$ km s^{-1}. *Bottom:* Integrated line emissivities for N v λ1240 (*dotted line*), C iv λ1550 (*long-dashed line*), [N ii] $\lambda\lambda$6548, 6584 (*short-dashed line*), and Hα (*solid line*). The shading identifies the different regions of the shock as described in the text.

We show the postshock temperature and density structure for protons and electrons in our model shock in the top panel of Figure 11. We assume a shock velocity of $V_s = 250$ km s^{-1}, characteristic of the shocks producing the radiation seen from spot 1 (Michael et al. 2000). The shock has a high Mach number ($M = V_s/c_s \gg 1$) and compresses the obstacle gas by a factor of $\sim$4 at the shock front, providing that the magnetic field is negligible. The temperature of the ions after crossing the shock front is given as $T_i = 3m_i V_s^2/16k$, where m_i is the mass of the ion and k is Boltzmann's constant. This implies that each ionic species will have a different postshock temperature, provided that there are processes to completely thermalize the postshock distribution functions. For collisional shocks, the postshock electron temperature is orders of magnitude lower than the ion temperatures (Zeldovich & Raizer 1967). On the other hand, in collisionless shocks, plasma turbulence (e.g., Cargill & Papadopoulos 1988) can partially equilibrate the postshock electron and ion temperatures. Eventually, the temperatures will be equilibrated by Coulomb collisions to a mean shock temperature $T_s = 3\mu m_p V_s^2/16k$, where $\mu = 4/(8 - 5Y)$ is the mean atomic weight per particle and Y is the mass fraction of helium.

In the region (the "ionization zone") immediately behind the shock front with a characteristic length of a few ionization lengths, the atoms are collisionally ionized. Since radiative processes in this region remove a negligible fraction of the thermal energy of the hot plasma, this part of the shock is called the "adiabatic" or "nonradiative" zone. Given sufficient time the radiative losses will remove the thermal energy and cause a runaway thermal collapse of the shocked gas. In order to maintain pressure equilibrium across the shock in this "cooling region," an increase in density will be accompanied by a temperature decrease in the region. Radiative cooling in the gas continues until its temperature ($T \approx 10^4$ K) is too low for the excitation of UV resonance lines, which are responsible for the rapid cooling. Moreover, once the gas starts to recombine, it quickly becomes optically thick to the ionizing radiation (mostly extreme UV lines) produced upstream in the cooling zone. Roughly half of this ionizing radiation propagates downstream and is reprocessed into optical emission lines in this "photoionization zone," where the gas is maintained at a temperature $T_c \approx 10^4$ K as a result of a balance between photoionization heating and radiative cooling.

The density of the gas in the photoionization zone is given by $\rho_c = 16\rho_0 T_s/3T_c$. For a $V_s = 250$ km s^{-1} shock, where $T_s \approx 10^6$ K, the gas in the photoionization zone can be compressed by a factor of $\approx$550. However, a significant magnetic field entrained in the gas may mitigate this compression (Raymond 1979).

Shocks that have developed cooling and photoionization zones are called "radiative shocks." A shock will be radiative if it has propagated for a characteristic cooling time $t_{\rm cool}$, which is defined as the time required for the shocked gas to cool from its postshock temperature to 10^4 K. Otherwise, we call it a "nonradiative shock." We calculate the

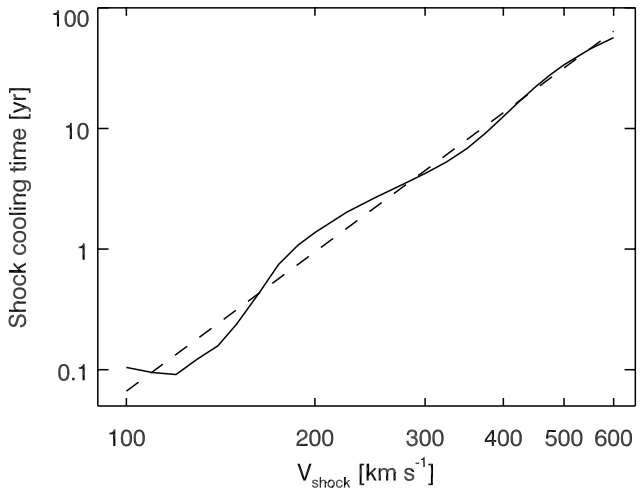

FIG. 12.—Model shock cooling time $t_{\rm cool}$ vs. shock velocity $V_{\rm shock}$ for initial obstacle density $\rho_0 = 2 \times 10^4$ amu cm^{-3} (*solid line*). The power-law fit $t_{\rm cool} \propto V_s^{3.8}$ (*dashed line*) is also shown.

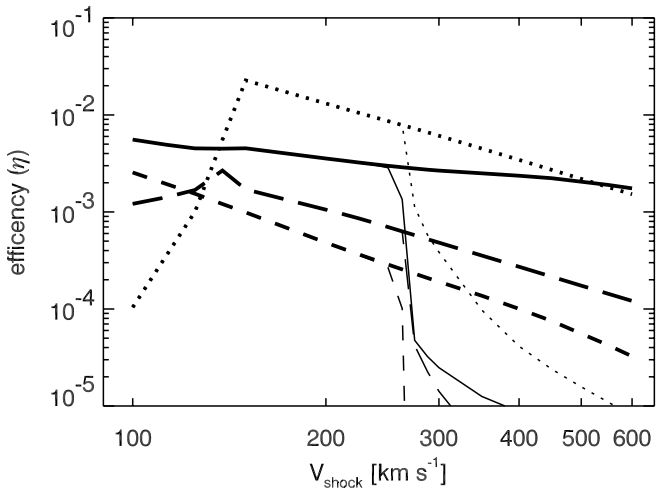

FIG. 13.—Line production efficiencies η for N v λ1240 (*dotted line*), C IV λ1550 (*long-dashed line*), [N II] $\lambda\lambda$6548, 6584 (*short-dashed line*), and Hα (*solid line*) as a function of shock velocity for fully cooled shocks (*thick lines*) and shocks that have only aged for 3 yr (*thin lines*).

cooling time $T_{\rm cool}$ for shocks in our models for input shock velocities $V_s = 100$–600 km s^{-1} and plot the results in Figure 12. We fit a power law to these results and obtain the relation

$$t_{\rm cool} \approx 2.2 \text{ yr} \left(\frac{2 \times 10^4 \text{ amu cm}^{-3}}{\rho_0} \right) \left(\frac{V_s}{250 \text{ km s}^{-1}} \right)^{3.8} ,$$

where ρ_0 is the preshock density. Therefore, for the range of shock velocities and preshock densities expected in spot 1, which was less than 4 yr old when our observations were made, some shocks may have already become radiative while others may remain nonradiative.

4.3. *Shock Emission*

After entering the shock front, atoms are collisionally ionized until they come into equilibrium with the postshock gas. These ions are collisionally excited and emit line radiation, some of which are from lower ionization stages than the final ionization state of a species. This ionization process in the ionization zone is not in equilibrium. Emission from this region leads to the detection of "Balmer filaments" in other SNRs (Hester, Danielson, & Raymond 1986; Long & Blair 1990). The Balmer emission comes from the shock front, where the H atoms are ionized.

When ions reach equilibrium with the postshock gas, the dominant line emission is in far-UV or soft X-ray wavelengths, depending on the postshock temperature. Most of the UV and optical line emissions are produced after the shock starts its thermal collapse. While the observed high-ionization UV lines are produced in the cooling region, the low-ionization UV and optical lines are produced in the photoionization zone, which is a dense H II region that is illuminated by the harder ionizing spectrum created upstream.

We plot the integrated surface emissivities of N v λ1240, C IV λ1550, [N II] $\lambda\lambda$6548, 6584, and Hα of our shock model described in § 4.2 as functions of downstream column density in the bottom panel of Figure 11. Most of these lines (>95%) are emitted during or after the thermal collapse of the shock, rather than in the ionization zone directly behind the shock front. Therefore, the resulting spectrum and magnitude of the emission from a shock depend greatly on whether the shock is radiative or nonradiative, and the cooling time of a shock is a good indication of the time it takes for a shock to "light up."

The luminosity of a line produced by a shock in units of ergs s^{-1} is given by

$$L = \tfrac{1}{2} \eta(V_s, \rho_0, t_{\rm shock}) \rho_0 V_s^3 A_s ,$$

where ρ_0 is the preshock density, V_s is the shock speed, $t_{\rm shock}$ is the age (time since first encounter) of the shock, and A_s is the surface area that the shock covers. The function η represents the fractional efficiency for a shock to convert its thermal energy into emission for a given line. As shown in Figure 11, η can be represented as a step function that turns on at $t_{\rm shock} = t_{\rm cool}$. We show the relation between the emission efficiency η and shock velocity V_s for several emission lines in Figure 13. The thick lines in Figure 13 represent shocks that have completely cooled, that is, $t_{\rm shock} \gg t_{\rm cool}$, while the thin lines are shocks with $\tau = 3(2 \times 10^4 \text{ amu cm}^{-3}/\rho_0)$ yr. Shocks with velocities $V_s > 250$ km s^{-1} have not yet cooled by $t_{\rm shock} = 3$ yr, and therefore their structures are truncated when compared to the fully developed radiative shocks. This shows again that radiative shocks are far more efficient radiators than nonradiative shocks. Therefore, while nonradiative shocks may be present in the protrusion, their net contribution to the observed UV and optical emission from spot 1 will be negligible.

For emission lines such as N v λ1240 (formed in the cooling region) and Hα (formed primarily in the photoionization zone), the line efficiency η has little dependence on the preshock density ρ_0. In contrast, forbidden lines are subject to collisional suppression, and therefore their emissivities are sensitive to ρ_0. The effect of suppression is illustrated in Figure 13 by the [N II] $\lambda\lambda$6548, 6584 lines, which have a critical electron density of $\sim 10^5$ cm^{-3} (Osterbrock 1989). Effects from collisional suppression increase as the shock velocity increases because faster

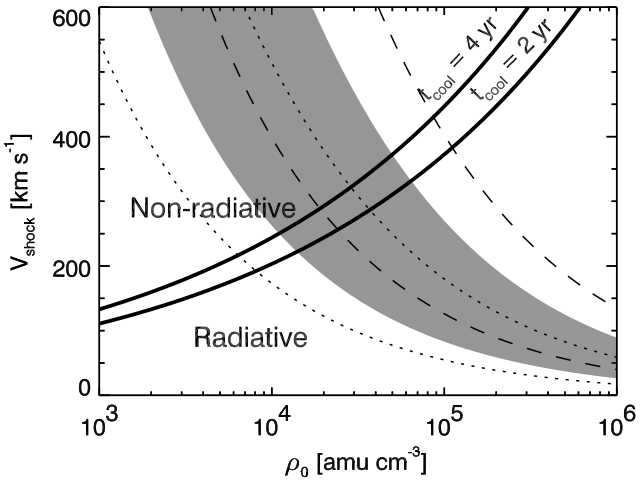

FIG. 14.—Similar to Fig. 10, with additional lines (*thick*) dividing the phase space between radiative shocks and nonradiative shocks for cooling time $t_{cool} = 2$ and 4 yr.

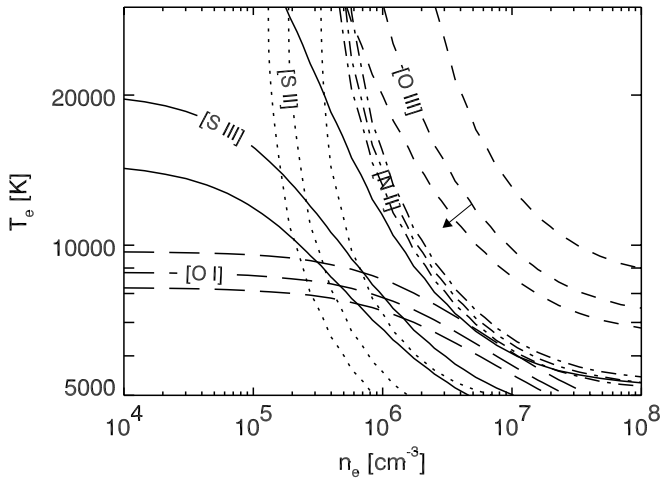

FIG. 15.—Contours of equal line ratios for [O I] $(\lambda\lambda 6300 + 6364)/\lambda 5577 = 18.5 \pm 4.2$ (*long-dashed line*), [O III] $(\lambda\lambda 4959 + 5007)/\lambda 4363 = 6.6 \pm 3.4$ (*short-dashed line*), [N II] $(\lambda\lambda 6548 + 6584)/\lambda 5755 = 2.0 \pm 0.2$ (*dot-dashed line*), [S II] $(\lambda\lambda 6717 + 6731)/(\lambda\lambda 4068 + 4076) = 0.1 \pm 0.04$ (*dotted line*), and [S III] $(\lambda\lambda 9068 + 9530)/\lambda 6312 = 20.7 \pm 10.9$ (*solid line*). The middle line corresponds to the determined ratio of the dereddened line fluxes, while the other two lines bracket the 1 σ errors. Since the [O III] $\lambda 4363$ line may be blended with some Fe emission, the measured ratio is a lower limit. The arrow attached to the [O III] ratio contours shows how this may affect the derived temperature and density.

radiative shocks generate more compression. Figure 13 also shows that line emissions such as N V $\lambda 1240$ can be produced only if the temperature of the shocked gas is high enough for that ion to be produced, as previously discussed in Michael et al. (2000). Above that threshold, the total line emissivity increases linearly with the shock velocity. Permitted emission lines formed in the photo ionization zone have a stronger dependence on shock speed, since they are generated by the reprocessing of the ionizing photons produced upstream in the cooling layer. For example, the Hα emissivity for fully developed radiative shocks increases approximately as $V_s^{2.4}$.

4.4. *Observed Shock Velocities and Preshock Densities*

Since the gas is relatively cool ($T \approx 10^4$ K) in the photoionization zone, the optical lines have thermal widths of order $10A^{-1/2}$ km s^{-1}, where A is the element's atomic mass. Macroscopic motion of the cooled layer will cause the observed line profiles of the optical lines to be significantly broadened. As the blast wave wraps around a protrusion, we expect to observe velocity components traveling both toward and away from us. The measured widths of the optical lines in the early *HST*/STIS spectrum suggest that the fastest radiative shock has a projected velocity of $\sim$250 km s^{-1} (Michael et al. 2000). Moreover, the observed line ratios of spot 1 indicate that lower velocity ($\lesssim$135 km s^{-1}) shocks must also be present (see § 5.2.1). Following the discussion in § 4.1.1, we are not surprised that a range of shock velocities is required to explain the observations.

Figure 14 shows the boundaries separating radiative and nonradiative shocks with t_{cool} of 2 and 4 yr overlayed on the hydrodynamically allowed regions of phase space for different values for the blast-wave pressure. In order for shocks with velocities as low as 135 km s^{-1} to be radiative, the density of the obstacle $\rho_0 \gtrsim 3 \times 10^4$ amu cm^{-3} has to be higher than most of the gas in the equatorial ring. A lower ρ_0 is needed if the blast-wave pressure is lower than our nominal estimate. While faster shocks propagating into less dense gas may also be present in spot 1, they do not contribute significantly to the observed optical and UV spectra because they are nonradiative.

5. ANALYSIS

5.1. *Nebular Analysis*

The *HST*/STIS spectrum of spot 1 consists of many forbidden emission lines of various species in the UV and optical wavelengths (see Tables 2 and 4). A standard nebular analysis on these data provides a good starting point because it indicates the typical values for the basic physical quantities that can be expected in the line-emitting region. We decide to focus our attention on the data taken around 1999 September (approximately day 4570) when a complete set of spectra is obtained from 1150 to 10270 Å. For each ion we consider a five-level model and include all relevant atomic processes, such as collisional excitation and de-excitation, and spontaneous radiative transitions. The atomic data of Osterbrock (1989) are used for the analysis, except for N IV, where the results from Ramsbottom et al. (1994) are used. We construct a grid of line ratios as functions of electron number density n_e and temperature T_e. Figure 15 shows the contours for which ratios of lines of [O I], [O III], [N II], [S II], and [S III] agree with the observed values.

The observed ratios of various forbidden lines require a relatively high electron density, $n_e \approx 10^6$ cm^{-3}, and temperature, $T_e \approx 10^4$ K. The upper limits for the line ratios of [N I] $(\lambda\lambda 5199 + 5201/\lambda 3467 < 0.11)$ and [O II] $(\lambda\lambda 3726 + 3729/\lambda\lambda 7320 + 7330 < 0.3)$ are consistent with the derived high n_e, as well as the N IV] $(\lambda 1483/\lambda 1486)$ line ratio. Recalling that the typical number density of the ring is $n \sim 10^4$ cm^{-3} (Lundqvist & Fransson 1996), our result indicates that the gas in spot 1 must have been compressed by a factor much greater than 4. This is consistent with our general picture (§ 4) that the UV and optical line emissions from spot 1 originate from a highly compressed gas behind a radiative shock. Our results also suggest the temperature and density stratification of the region where these emission lines are formed. This is also consistent with our general picture

for radiative shocks where emission lines from different ionic species are created in different regions of the shock.

As discussed earlier (§ 4.3), the optical emission lines from a radiative shock come from a photoionization zone in the cooled postshock gas. This photoionization picture is supported by the observed Balmer decrement in spot 1, $H\alpha : H\beta : H\gamma : H\delta = 3.63(\pm 0.21) : 1 : 0.48(\pm 0.06) : 0.24 (\pm 0.04)$, which is generally consistent with both case A and case B values typically seen in photoionized gaseous nebulae (Osterbrock 1989). A complete analysis of the H and He lines will be presented in C. S. J. Pun et al. (2002, in preparation).

5.2. *UV Emission Line Modeling*

Emission lines from the higher ionization stages (e.g., N IV, C IV, O IV, N V) are formed in the cooling region of a shock, where the gas temperature and density are stratified and the ionization levels can be out of equilibrium. However, within each ionization stage, the populations of all energy levels are in equilibrium. We model these lines with a radiative shock code that properly accounts for these effects. We compare our model results with the observations of six UV emission lines detected with the G140L grating (N V $\lambda\lambda$1238, 1243, Si IV λ1393, 1403, O IV] λ1400 multiplet, N IV] λ1486, C IV $\lambda\lambda$1548, 1543, and He II λ1640). We choose these lines because they have negligible contamination from the ring emission and because they have been observed at three different epochs from day 3869 to day 4596. We decide not to model the Mg II $\lambda\lambda$2796, 2803 doublet, the strongest emission line in the spot 1 spectrum, because of the large uncertainties in the observed flux (over a factor of 2; see Table 4), caused by huge interstellar Mg II absorption along the LMC line of sight (see § 3.3). Moreover, with the Mg II line flux being measured in only one epoch, we are not able to monitor its time evolution as for the other far-UV lines. Similarly, we have not attempted models to fit both the UV and the optical emission lines because of the limited time and wavelength coverage of the optical data (see Table 2).

For a given set of input shock model parameters (shock velocity, preshock density, and abundances), we follow the evolution of the downstream gas until the shocked gas has cooled to 5000 K. We store the integrated flux for various emission lines at intermediate grid points behind the shock as the basic vectors by which we compare with the observed data. We then vary the parameters in the models to obtain the best fit. To seek the best fit, we allow the abundances to vary from our standard "ring" abundance described in § 4.2.

5.2.1. *Single-Shock Models*

Using a grid of single-shock models with $V_s = 100$–400 km s^{-1}, we were unable to reproduce the emission-line fluxes and widths observed from spot 1 at any epoch. One of the main challenges for the single-shock model is to explain the relatively low ratios of N V λ1240 flux to the fluxes of lines from lower ionization stages (e.g., N IV] λ1486 and C IV λ1550) in light of the widths ($\approx$250 km s^{-1}) of the observed lines. The abundance of N V increases rapidly for shock velocities exceeding $\approx$135 km s^{-1}, while N IV and C IV are present at lower shock velocities (see Fig. 13). As a result, the model line ratios N V λ1240/C IV λ1550 $\approx$ 10 and N V λ1240/N IV] λ1486 $\approx$ 8 for shocks faster than 135 km s^{-1} exceed the observed ratios of 0.6–1.7 and 2.5–5.6, respectively. The fact that this discrepancy exists for both line ratios indicates that this result does not depend on our choice of abundances. We therefore conclude that a single-shock model cannot reproduce the observed line emissions of spot 1, as in our earlier studies (Michael et al. 2000).

5.2.2. *Two-Shock Models*

We are not too surprised that single-shock models fail to fit the observed emissions from spot 1 because we expect a range of shock velocities V_s in the interaction (see § 4.1.1). The exact distribution of V_s depends on the geometry and density distribution in the obstacle, which are both unknown. Rather than attempting to explore the vast parameter space of possible shock velocity distributions, we fit the observed line emissions with models consisting of only two distinct shocks, each having a different velocity and surface area. We explore parameter space with shock velocities ranging from 100 to 400 km s^{-1} and find reasonable fits to the relative line strengths with a combination of one "slow" shock with $V_s = 135$ km s^{-1} and one "fast" shock with $V_s = 150$–400 km s^{-1}. As discussed below in § 5.3, the observed line profiles suggest that the fastest radiative shocks have velocities $V_s \approx 250$ km s^{-1}. We therefore assume this value for the fast shock component.

The hydrodynamic simulations shown in Figure 8 illustrate two possible scenarios to account for the observed increase of the line fluxes with time. The crucial parameter distinguishing these scenarios is the ratio $t_{\rm shock}/t_{\rm cool}$, where $t_{\rm shock}$ is the "age" of the interaction (i.e., the time since first impact) and $t_{\rm cool}$ is the characteristic radiative cooling time for the transmitted shocks. For the case in which both the blast-wave pressure and the obstacle density are low, $t_{\rm shock} \approx t_{\rm cool}$ and the shocks in the obstacle would be in the process of developing their radiative layers. In this scenario the observed increase of the line fluxes is due primarily to the development of new radiative layers as the shocks age. Alternatively, for the case in which the density of the obstacle is high, $t_{\rm shock} \gg t_{\rm cool}$ and the shocks quickly become radiative. The observed increase of the line fluxes is then due to the increase in the surface area of the shocks as the blast wave overtakes more of the obstacle. We suspect that we are observing a combination of these two behaviors. Given our limited data set (six lines in three epochs), we decide to fit only two limiting models that probably bracket the actual situation: evolution due solely to shock aging (model 1) and evolution due solely to increasing shock areas (model 2).

For model 1 we assume that the area of each shock remains constant over time and the only fitting parameters are the surface area and age of each of the two shocks. We assume that the faster shock is older because it represents the head-on shock that appears when the blast wave first encounters the obstacle and that the slower shock is younger because it is driven into the sides of the obstacle by an oblique blast wave at a later time. For this model we need to assume a low preshock density $n_0 = 10^4$ cm^{-3} so that $t_{\rm cool} \approx t_{\rm shock} \approx 3$ yr for the fast shock. We also assume that the preshock density is constant throughout the obstacle for both models. The best-fit model for model 1 has $\chi_r^2 \approx 1.6$, and its parameters are listed in Table 5. The model (*squares*) and observed (*error bars*) fluxes for all six emission lines are plotted in Figure 16. For the best-fit model, the surface area of the slower shock needs to be $\sim$4 times greater than that of the faster shock to fit the low observed N V λ1240/C IV

TABLE 5
TWO-SHOCK MODEL RESULTS

Model Parameters[a]	Model 1 $n_0 = 10^4$ cm^{-3}	Model 2 $n_0 = 3.3 \times 10^4$ cm^{-3}
τ_{135} (yr)	0.03 ± 0.01	...
τ_{250} (yr)	2.21 ± 0.01	...
$A_{135}A_{250}$	3.6 ± 0.7	...
$A_{135}A_{250}(1)$	...	5.9 ± 3.3
$A_{135}A_{250}(2)$	...	3.3 ± 1.2
$A_{135}A_{250}(3)$	...	2.8 ± 0.9
He	1	1
C	1.85 ± 0.59	2.06 ± 0.66
N	0.55 ± 0.08	0.54 ± 0.08
O	0.83 ± 0.16	0.75 ± 0.14
Si	1.15 ± 0.37	0.78 ± 0.24

[a] The model parameters from top to bottom: (model 1) age of each shock at the first observation epoch, ratio of shock surface areas; (model 2) ratio of shock surface areas for the three observations (day 3869, day 4388, day 4596); (models 1 and 2) abundances adjustment factor with respect to the "ring" abundances (see § 4.2). The He abundance is kept fixed for both models.

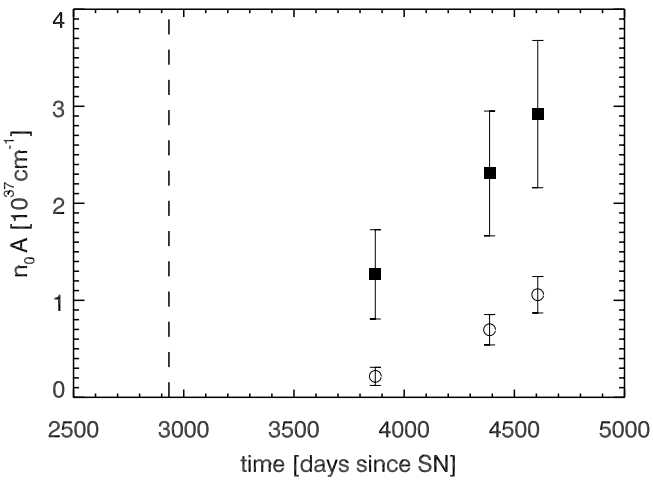

FIG. 17.—Shock area growth for the $V_s = 135$ km s^{-1} (*filled squares*) and $V_s = 250$ km s^{-1} (*open circles*) shocks in the best-fit model 2 scenario. The dashed line shows the earliest date (day 2932) that spot 1 appeared as reported by Lawrence et al. (2000a).

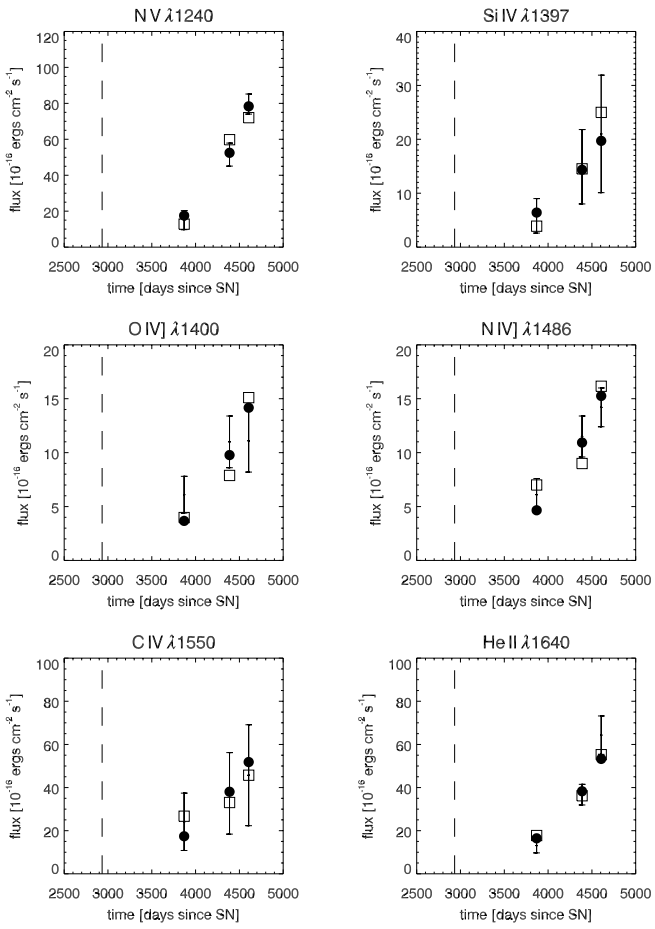

FIG. 16.—Observed (*error bars*) and modeled (model 1: *open squares*; model 2: *filled circles*) light curves for the UV lines. The dashed line shows the earliest date (day 2932) that spot 1 appeared as reported by Lawrence et al. (2000a).

λ1550 flux ratio. In this model, the fast shock was 2.2 yr old at the time of the first UV observation (day 3869), while the slower shock was only 1 week old. The age of the fast shock is only slightly smaller than the results of Lawrence et al. (2000a), who suggest that spot 1 was at least 2.6 yr old by the time of our first UV observation. This pleasant result is offset by the suspiciously young age of the slower shock.

For model 2 we assume that the preshock density is high enough so that all the shocks are fully radiative at all epochs. The fitting parameters for this model are the areas of the two shock surfaces at each of the three observation epochs. We find that the quality of the fits is rather insensitive to the assumed preshock density ($n_0 = 3.3 \times 10^4$ cm^{-3} is assumed). This is true because the six UV lines we are fitting are not subject to collisional suppression (including N IV] λ1486, for which $n_{\rm crit} > 3 \times 10^9$ cm^{-3}), so their emission efficiencies η do not depend on the preshock density (see § 4.3). The luminosities of such lines are actually proportional to the product $n_0 A$ of the preshock density and shock area. We present the best-fit parameters of the model in Table 5 and the model line fluxes in Figure 16 (*circles*). Since model 2 provides a better statistical fit ($\chi_r^2 \approx 1$) to the observed line strengths than model 1, we conclude that the increase of shock areas is the dominant cause of the increase of the fluxes.

Figure 17 shows the time dependence of the fitted shock areas (actually the product $n_0 A$) for model 2. Similar to model 1, we find that $\sim$4 times more surface area must be covered by the slow shocks than by the fast shocks. While our best-fit model results are statistically consistent with a constant ratio of slow to fast shock area ($A_1 35 : A_2 50$ in Table 5), they suggest that this ratio may be decreasing with time. This behavior is not what we would expect from simple protrusion models shown in Figure 8. In such models the fast shocks are created first and only the area of slow shock interaction increases as the blast wave overtakes more of the obstacle. One possible explanation is that there may be many protrusions or clouds distributed in spot 1 and therefore the net area of fast shocks can increase with time

as more of them are encountered by the blast wave. Another possible explanation arises from the fact that model 2 by construction does not allow for any aging of shocks. However, the real light curve of the spot 1 emission is probably a combination of increased shock areas and additional emission from older, but newly cooled, radiative shocks. The addition of fast shock area at later times seen in model 2 can therefore be attributed to shocks that were created before our first observation but added their emission later after they had cooled and become radiative.

Our finding that more area is covered by the slow shocks than fast shocks suggests that the obstacle may have an elongated shape with an aspect ratio $\approx A_{\rm slow}/A_{\rm fast}$, where $A_{\rm slow}$ and $A_{\rm fast}$ are the shock areas for the slow and fast shocks, respectively. Assuming a simple, hemispherical geometry for the obstacle, we estimate that it has a typical scale length of $d_{\rm spot} \approx [2(A_{\rm slow} + A_{\rm fast})/\pi]^{1/2}$. We find a best-fit size of the obstacle $d_{\rm spot} \approx 2 \times 10^{16} (3.3 \times 10^4 \ {\rm cm}^{-3}/n_0)^{1/2}$ cm at day 4606, the time of our last STIS observation. This is consistent with our finding (see § 2) that spot 1 remains spatially unresolved in our data.

While the two-shock models successfully fit the time evolution of the UV emission lines, these models fail to account for the observed fluxes of the optical lines (e.g., Hα, Hβ, [N II] $\lambda\lambda$6548, 6583, [O I] $\lambda\lambda$6300, 6364, and [O III] $\lambda\lambda$4959, 5007) emitted in the photoionization zone (§ 5.1). The observed optical fluxes are typically factors of 2–3 greater than those predicted by our models. We exclude emission from the precursor as a possible contributor to the extra emission because its emission would be narrow and center at zero velocity. However, we exclude that portion of the line profile when we fit the spot 1 medium-resolution G750M data (see Fig. 4). We discuss other possible explanations for this discrepancy in § 6.

Finally, we emphasize that the satisfactory fits of the UV line fluxes were possible only if we allow abundances to vary from our standard "ring" abundance. The inferred abundances are roughly consistent with the ring abundances inferred by Lundqvist & Fransson (1996), but differences as large as a factor of 2 are derived.

5.3. *Line Widths and Profiles*

In this section we discuss what can be learned from the widths and profiles of the observed emission lines. The data are sparse. We measure line widths of spot 1 accurately for only a few optical lines (see § 3.2). We also only have rough estimates of the widths of a few far-UV lines (see § 3.3.3).

The line widths and profiles are dominated by the shock dynamics and not thermal broadening. The line-emitting gas behind a radiative shock travels at approximately the shock speed and will therefore emit line radiation with a Doppler shift determined by the line-of-sight velocity of the shock. For emission lines originated from the photoionization zone ($T \approx 10^4$ K), e.g., the optical forbidden lines, the thermal broadening is $\sim 10 A^{-1/2}$ km s^{-1}, which is much smaller than the observed widths of the lines ($\sim$250 km s^{-1}). The thermal broadening for emission lines formed in the cooling region, such as N v λ1240, while larger than that for the optical forbidden lines, is still much smaller than the dominating Doppler broadening effects of the macroscopic motions of the shock. Although it is poorly measured, the width of the N v λ1240 line (Table 4) appears to be higher than that of all the other optical and UV emission lines, with the possible exception of Hα. This result can also be explained by Figure 13, which shows that the N v λ1240 emission can only be produced in shocks faster than $\approx$135 km s^{-1}, while all the other lines can be produced by even slower shocks.

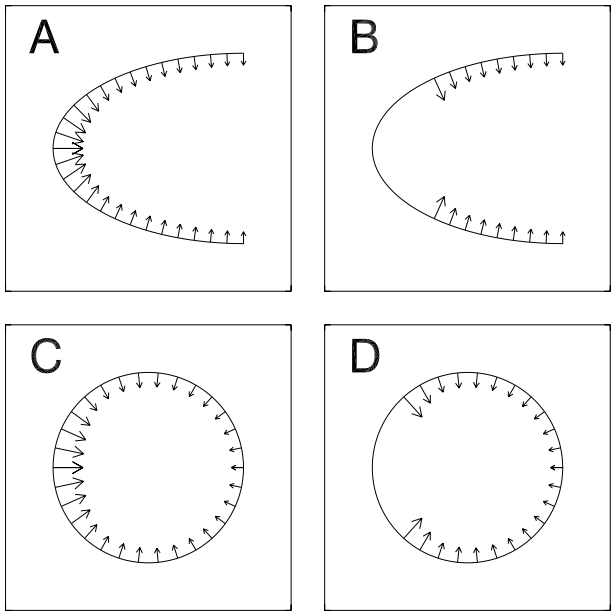

FIG. 18.—Model shock-front geometries and flow fields for the radiative shocks in the obstacle (shock incident from the left side). The shock speed varies along the surface from 250 km s^{-1} at the front to 100 km s^{-1} at the back. Cylindrical symmetry is assumed for all models.

The fact that the measured widths of the [O I], [N II], and [S II] lines are smaller than Hα (Table 3) indicates that the faster shocks produce these lines with lower efficiencies (compared to Hα) than the slower shocks. This is caused by collisional suppression of the forbidden lines, which increases with increasing compression ratio of the photoionized zone, as shown previously in Figure 13.

The line profile shapes depend on the geometry of the shock surface and its orientation relative to the observer. The shocks having the highest projected velocities toward and away from the observer produce the blue and red wings of the lines, respectively. The Doppler shifts of the wings of the line profile therefore provide a lower limit to the velocity of the fastest radiative shocks present while both fast transverse shocks and slow shocks contribute to the cores of the line profiles.

We construct simulated Hα line profiles based on simple geometries for the protrusion (e.g., Fig. 8) in order to derive constraints on the hydrodynamics model of the interaction. The 1999 August 30 (day 4568) G750M 0$''$.1 line profile of Hα is chosen because it is well observed and is not affected by collisional suppression. Figure 18 shows our model shock surface geometries. For each model we assume a distribution of shock velocities (from 100 to 250 km s^{-1}) normal to the surface of the protrusion. We normalize each velocity distribution by requiring that the relative areas of fast ($V_s > 135$ km s^{-1}) and slow ($V_s < 135$ km s^{-1}) shocks in each model are $\approx$4, as determined from the best-fit two-shock models (§ 5.2.2). We also assume that the axis of symmetry of the protrusion points radially inward from the circumstellar ring at the location of spot 1 for all models. We

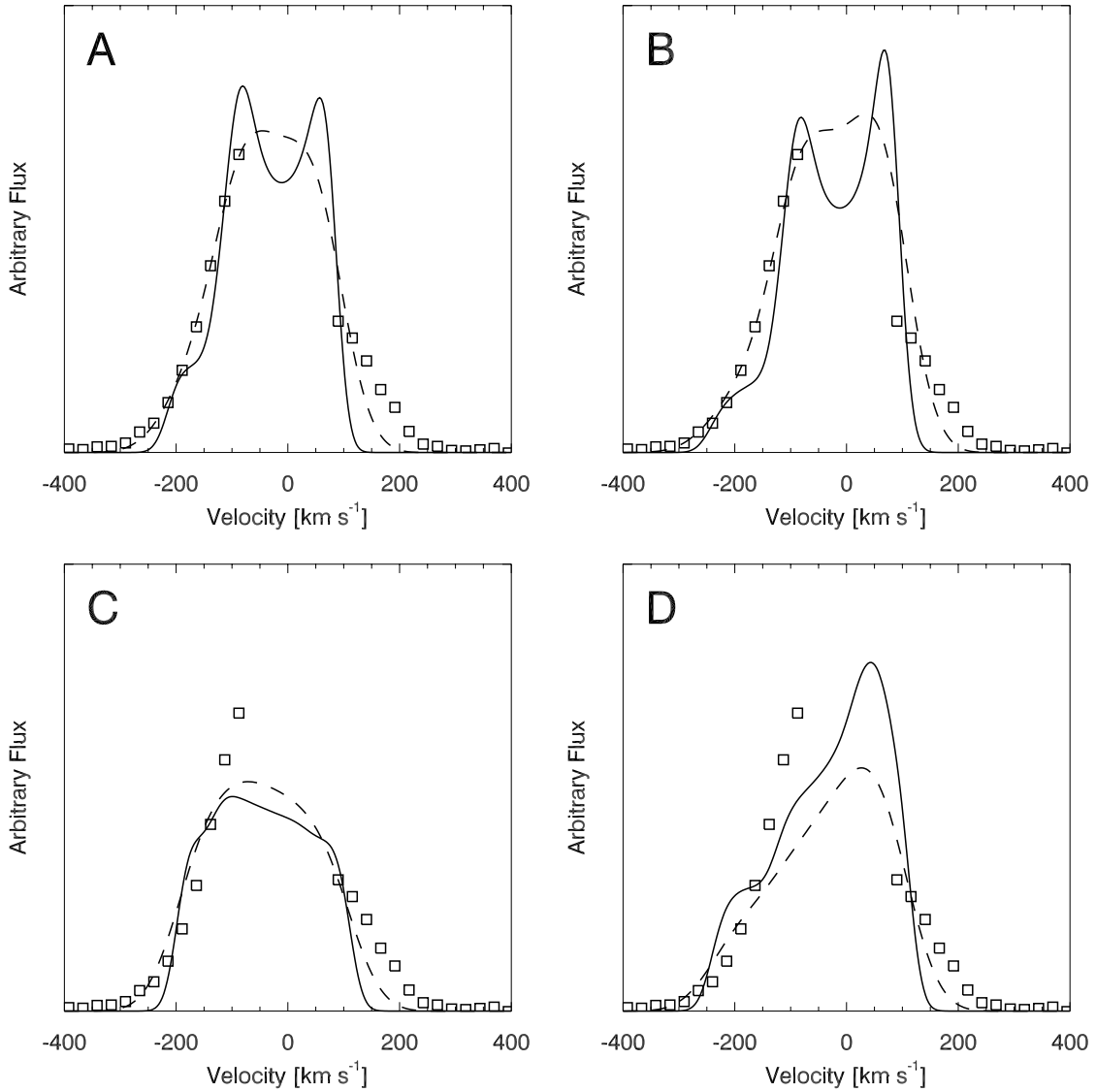

FIG. 19.—Model Hα line profiles (*solid line*) for the shock-front geometries in Fig. 18. These profiles are smoothed with a Gaussian of FHWM = 100 km s^{-1} (*dotted line*). The day 4568 Hα line profile from the medium-resolution 0$''$.1 G750M data is plotted for comparison (*squares*). The uncertainties of the observed profile are smaller than the size of the symbol. The low-velocity region (-50 to 50 km s^{-1}) is dominated by emission from the circumstellar ring (see Fig. 4) and is therefore not displayed.

calculate line profiles by convolving the surface emissivity ($\propto V_s^{2.4}$; see § 4.3) of the radiative shocks with the fractional areas covered by shocks having the appropriate line-of-sight velocities. We then convolve the model profile with the STIS LSF (Leitherer et al. 2000). At the Hα wavelength, the STIS LSF for the G750M 0$''$.1 aperture can be well approximated with a Gaussian of FWHM = 1.5 pixels. The simulated profiles are finally normalized for comparison with the observed Hα profile.

Figure 19 shows the resulting Hα line profiles (*solid line*) from the geometry models of Figure 18. For each case the day 4568 Hα profile (*squares*) is also plotted for comparison. The observed line width indicates that radiative shocks are present with projected velocities of $\approx$250 km s^{-1}, which is a good indication of the velocities of the fastest radiative shocks present. The line profile formed from an ellipsoidal model surface (model A) has multiple peaks and steep edges that are not apparent in the observed profiles. The peaks are due to caustics in velocity space that occur where the shock surface lies tangent to the plane of the sky. These features are less pronounced in the line profiles produced by a spherical model surface (model C), where tangential surfaces comprise a lower fraction of the total surface areas.

For each case we also show a model in which no radiation comes from the tip of the protrusion (models B and D, for elliptical and spherical surfaces, respectively). These models are motivated by the observations from the *Chandra X-Ray Observatory* (Burrows et al. 2000; Park et al. 2002), which show a bright spot in the X-ray image of SN 1987A coincident with spot 1. One possible interpretation is that the X-rays come from a faster ($V_s > 600$ km s^{-1}) nonradiative shock at the tip of the protrusion responsible for spot 1. We notice that this picture is also consistent with one where there is a density gradient across the ring.

While the model line profiles have similar widths as the observed Hα line, they do not provide a good fit in the high-velocity portion ($\gtrsim 100$ and $\lesssim -150$ km s^{-1}) of the line profile. As we shall discuss in § 6, radiative shocks are subject to instabilities that will introduce "turbulence" in the radiative layer. We simulate the effect of this turbulence qualitatively by convolving the derived model line profiles with Gaussians of FWHM = 100 km s^{-1}. The resulting line profiles (dashed lines in Fig. 19) provide substantially better matches to the observed Hα line.

6. DISCUSSION

While the idealized radiative shock models described in §§ 4 and 5 provide a plausible framework for interpreting the spectrum of spot 1, they do not account for all the details of the observed line ratios and profiles. In this section we consider what the departures of the actual spectra from the model spectra may tell us about how the actual physical situation differs from our models.

First, we discuss the "turbulent" broadening that we introduce in § 5.3 to make the model line profile resemble the observed one at high velocity. This turbulence is almost certainly due in part to the cooling instabilities that exist behind radiative shocks with $V_s \gtrsim 150$ km s^{-1} (Chevalier & Imamura 1982; Imamura, Wolff, & Durisen 1984; Innes, Giddings, & Falle 1987; Strickland & Blondin 1995; Walder & Folini 1998). To illustrate the effects of these instabilities, we construct a one-dimensional VH-1 simulation of a blast wave driving a radiative shock into gas of constant upstream density, $n_0 = 3.3 \times 10^4$ cm^{-3}, and the results are shown in Figure 20. In the figure, the upstream gas flows to the left with a velocity $V_{\rm inflow} = 220$ km s^{-1} while the radiative gas, shown as a dark band, propagates to the right with a mean velocity of $\sim$250 km s^{-1}. The dark gray parabolas represent the positions of the actual shock front, which moves ahead of the radiative layer and then collapses back to the radiative layer over time. The velocity of the shock front relative to the upstream gas varies from $\sim$100 to 300 km s^{-1}. This process repeats itself on a timescale comparable to the cooling time of the shocked gas. In our simulation, the forward shock never stabilizes while the oscillation of the velocity of the radiative layer decreases as it gains mass with time.

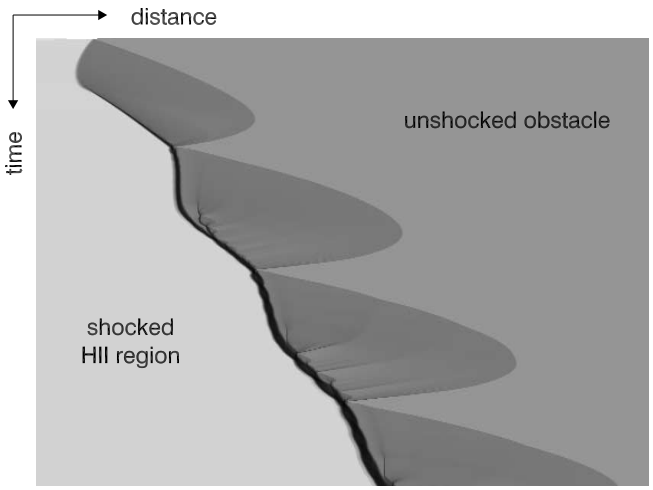

FIG. 20.—One-dimensional VH-1 simulation (800 spatial zones) of a radiative shock ($V_s \approx 250$ km s^{-1}) developing in a dense ($n_0 = 3.3 \times 10^4$ cm^{-3}) obstacle. Shown is a space-time diagram where darker shade represents higher density. The overall flow is advecting to the left as a result of the inflow boundary conditions chosen for the right-hand side boundary ($V_{\rm inflow} = 220$ km s^{-1}).

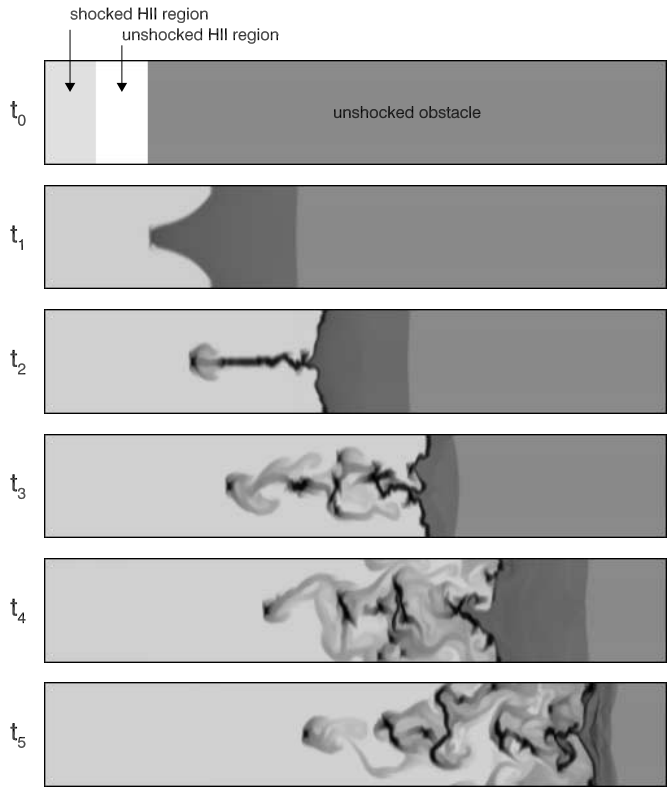

FIG. 21.—Two-dimensional VH-1 simulation (80 × 400 zones) of the development of a "turbulent" cold layer behind a radiative shock ($V_s \approx 250$ km s^{-1}) in a dense ($n_0 \approx 3.3 \times 10^4$ cm^{-3}) obstacle. The elapsed time between individual frames is 1 yr. The obstacle has an imposed 5% sinusoidal density perturbation in a direction perpendicular to the shock front.

The instabilities that exist behind radiative shock become more dramatic in the two-dimensional simulations, as described in Walder & Folini (1998). We construct a two-dimensional VH-1 shock simulation in Figure 21 to illustrate such effects. We introduce a 5% sinusoidal density perturbation of the unshocked gas in a direction perpendicular to the shock front, with the perturbation wavelength comparable to the cooling length of the transmitted shock. As the shock enters the dense gas, a Richtmyer-Meshkov instability develops rapidly at the contact discontinuity. After several cooling times (and forward shock oscillations), the radiative layer is shredded into a chaotic flow of tiny blobs by a combination of thermal and Rayleigh-Taylor instabilities.

If the blast wave strikes the obstacle at oblique incidence, the flow of shocked gas parallel to the contact surface will cause strong Kelvin-Helmholtz instabilities to shred the surface even further and will introduce a component of velocity parallel to this surface in the radiative layer. We can see these instabilities beginning to develop in the last frames of Figure 8. However, we have not attempted to model their consequences in our simulations of the line profiles.

Since *HST* only allows us to resolve structures with dimensions $\gtrsim 10^{17}$ cm at the distance of SN 1987A, we have no direct knowledge of the actual shape or the density distribution of the protrusion gas responsible for the spot 1 emission. Even in the case in which it has a simple shape such as that shown in Figure 8, the instabilities discussed above will introduce turbulent structures at scale lengths of $\sim 10^{13}$ cm, which we cannot hope to resolve with current technology.

Moreover, it is unclear whether the assumption that the protrusion gas has a simple shape with a smooth surface is justified. While we know that the circumstellar ring has a range of densities (Lundqvist & Fransson 1996), we do not know the scale lengths on which these inhomogeneities may be distributed. If the blast wave encounters a "lumpy" medium, a complex flow will develop where the radiating blobs are hammered both by the reflected shocks and by the blast wave itself. Clearly, the current observations allow for many plausible scenarios for the hydrodynamics of the radiating gas for which quantitative models are beyond the scope of this paper. We are not surprised that the simple hydrodynamic models we have considered in § 5.3 fail to reproduce the observed line profiles.

Magnetic fields may also affect the shock dynamics. For the range of densities and shock velocities expected in spot 1, we estimate that a magnetic field with strength $B_0 \gtrsim 400$ μG entrained in the upstream gas would be sufficient to suppress compression in radiative shocks and stabilize the cooling instabilities (Innes 1992). This will result in a photoionization zone of lower density.

In our idealized shock models of §§ 4 and 5, we have only considered radiative shocks in which the pressure driving the shocks is constant. However, as Borkowski et al. (1997b) and Luo et al. (1994) have shown, the pressures behind an actual blast wave encountering an obstacle have a complex time dependency. As the reflected blast wave travels away from the surface of the obstacle, the flow diverges and the driving pressure decreases. Later, the pressure driving the radiative shock into the obstacle may suddenly rise again owing to "echo" shocks produced when the reflected shock strikes the contact discontinuity and the reverse shock.

The most troubling failure of our models is their inability to account for the observed ratio of fluxes of optical to UV lines. As we have described, the radiative shock models consistently predict optical fluxes that are factors of ≈ 3 lower than expected from models that are normalized to give the observed UV line fluxes.

A simple way to account for the discrepancy between the observed and model optical/UV line ratios is to assume that the extinction of spot 1 is greater than that previously determined for SN 1987A. If we applied a reddening of $E(B-V) \approx 0.23$, the corrected UV flux would increase by a factor of ≈ 3, sufficient to remove the discrepancy. Considering that spot 1 is located on the far side of the ring from the observer, a column density $n\ell \approx 10^{21}$ cm^{-2} of gas with a 30 Doradus dust/gas ratio in the foreground of spot 1 (perhaps the ring material itself) could account for such additional reddening. It is also possible that the shock itself may destroy graphite dust grains and elevate the ratio of C/N abundances in spot 1 (compared to the unshocked ring) to account in part for the relatively low observed ratio of N v λ1240/C iv λ1550. Shocks faster than ≈ 200 km s^{-1} can destroy graphite grains in a timescale $\lesssim 2$ yr (Tielens et al. 1994).

The revised value of $E(B-V)$ is 0.04 (and 2 σ) greater than the measurement of 0.19 ± 0.02 by Scuderi et al. (1996) on the nearby star 2 and 0.07 greater than the value we adopted for Table 4. However, modeling of the UV and optical narrow emission lines for the inner circumstellar ring by Lundqvist & Fransson (1996) does not support such a large $E(B-V)$ value. Therefore, we do not regard it to be highly probable.

A second way to account for the optical/UV line ratio is the presence of an extra source of ionization in the photoionization zone that is roughly 3 times stronger than the radiation from the shocked gas itself. In the one-dimensional radiative shock models described in § 4, the only source of ionizing radiation for the photoionized zone is the shocked gas immediately upstream from that layer. One possible candidate for the extra ionization is the faster shocks that have not had time to develop their own radiative layers. However, we are not confident that such models will work. The problem is that the presumed extra ionizing radiation must also illuminate the cooling zone where the UV emission lines are formed, and this illumination will elevate the abundance of N v in the cooling layer. As a result, shocks with velocity $V_s \lesssim 135$ km s^{-1} will produce extra N v λ1240 emission, causing the predicted N v λ1240 flux to again exceed the observed value. A more promising candidate for the extra source of ionization is the nonthermal radiation from particles accelerated in the shock itself. Detailed modeling is required to demonstrate its feasibility.

A third possible explanation for the failure of the models to account for the ratios of optical to UV emission lines is the inadequacy of the stationary radiative shock models themselves. Our findings are similar to that from the modeling of the spectra of Herbig-Haro objects with simple plane-shock and bow-shock models, where high-ionization lines, such as C iv and N v, are underproduced (Böhm & Goodson 1997). As we have shown in Figure 21, radiative shocks are inherently unstable and the ratio of optical to UV emission lines from such unstable shocks may be different from that in a stationary flow, even in a time-averaged or ensemble-averaged sense. For example, the temperature gradients in the unstable flow are more pervasive than in a stationary flow, in which case thermal conduction may provide an additional energy source.

Future observations with the *HST* may be very helpful in resolving some of the issues that we have raised here. Valuable clues to resolving the optical/UV line ratio puzzle may come from observations of the same ratio in the other hot spots. For example, if the ratio is affected by extinction by dust in the immediate foreground of spot 1, it might have different values in the other spots, some of which lie on the near side of the circumstellar ring.

We can also benefit from observations of the UV emission lines at a higher spectral resolution. First, we can better estimate the amount of flux reduction caused by the LMC interstellar absorption (see § 3.3.3) by obtaining the line profile shapes of emissions not affected by this absorption, such as N v λ1240 and N iv $\lambda\lambda$1483, 1486. This will significantly reduce the error estimates of the measured fluxes affected by this absorption, especially for Mg ii λ2800, where the flux correction due to LMC absorption applied is both the highest and the most uncertain. Second, to reconcile the observed low flux ratio of N v λ1240/C iv λ1550, we have suggested a two-shock model in which the higher velocity radiative shocks make up a relatively small fraction of the

shock area compared to the lower velocity shocks. This model implies that the ratio of N v λ1240/C iv λ1550 line emissivity should increase in the wings of the lines, where only the fastest shocks contribute. On the other hand, we have also suggested that destruction of graphite grains in the faster shocks may elevate the abundance of carbon in the gas phase and lead to a decrease in the ratio of N v λ1240/C iv λ1550 in the wings of the lines. However, as shown in Figure 6, the observed profile of C iv λ1550 is severely modified by interstellar absorption, introducing large uncertainties in the N/C abundance ratio. We may get a clear look at the red wing of C iv λ1550 by observing the spots on the far side of the ring (e.g., spots 3, 4, and 5), where the shock emission would be mostly redshifted to wavelengths where the interstellar absorption is not so severe. When spot 1 becomes bright enough to permit observations of the line profile of N iv] λ1486, the flux ratio of N iv] λ1486/N v λ1240 as a function of position within the line profile will give us a diagnostic of shock excitation versus velocity that is independent of relative abundances and not subject to interstellar absorption.

7. SUMMARY

In conclusion, we summarize the main results of this paper:

1. We describe the *HST*/STIS UV and optical spectrum of spot 1 up to day 4606 (1999 October 7). We measure and tabulate fluxes, line widths, and line centroids for all lines detected in the spectrum.

2. We determine correction factors to account for the substantial interstellar line absorption of several lines (C ii λ1335 multiplet, Si iv $\lambda\lambda$1394, 1403, C iv $\lambda\lambda$1548, 1551, and Mg ii $\lambda\lambda$2796, 2803). However, these factors are poorly constrained because of uncertainties in the line widths and centroids.

3. The observed emission is caused by radiative shocks that develop when the supernova blast wave strikes dense gas protruding inward from the equatorial ring. A nebular analysis of several line ratios confirms that many of the emission lines are formed in a region of very high density gas ($n_e \sim 10^6$ cm^{-3}), which has been compressed by factors $\gtrsim$100 as a result of radiative cooling downstream from the shock.

4. The observed line widths indicate that radiative shocks with velocities as high as 250 km s^{-1} are present, while the line ratios indicate that much of the radiation must come from slower shocks ($V_s \lesssim 135$). The inferred range of shock velocities is a natural consequence of a model in which a blast wave overtakes a dense obstacle.

5. Hydrodynamic arguments show that such slow shock velocities will be present only if the density in the unshocked obstacle is sufficiently high ($n_0 \approx 3 \times 10^4$ cm^{-3}). This density lies at the high end of the range of densities observed for the ring by Lundqvist & Fransson (1996). The fact that shocks with velocity $V_s = 250$ km s^{-1} must have become radiative after 3 yr sets a lower density limit, $n_0 \gtrsim 10^4$ cm^{-3}.

6. Faster shocks ($V_s \approx$ 250–1000 km s^{-1}) may also be present in spot 1, as would be the case for shock interaction with the lower density gas ($n_0 < 10^4$ cm^{-3}) present in the ring (Lundqvist & Fransson 1996). These shocks would be invisible in the optical and UV emission spectra though because they would not yet have developed radiative layers. However, they may contribute to the enhancements of X-ray emission seen near the hot spots by the *Chandra X-Ray Observatory* (Burrows et al. 2000; Park et al. 2002).

7. We interpret a subset of the observed emission lines (six UV lines observed at three epochs) with a model consisting of two one-dimensional stationary radiative shocks with different velocities ($V_s = 135$ and 250 km s^{-1}). In our favored model, the lines brighten because the area of the obstacle overtaken by the blast increases with time. The area covered by the slower shocks must be $\approx$4 times that covered by the faster shocks. To account for the observed line strengths, the obstacle must have a characteristic scale length of 2×10^{16} cm.

8. Our models underestimate the ratio of observed optical/UV line fluxes by a factor of $\sim$3. This may indicate the presence of an additional source of ionizing flux in the photoionization zone or that the assumption of steady state shocks is too limiting.

9. The observed line profiles are in qualitative agreement with simulated profiles created from simple geometries for the obstacle. The nearly Gaussian observed profiles indicate the presence of chaotic flows in the photoionized region, caused by violent thermal and shear instabilities in the shocked gas.

10. Continued UV and optical observations of spot 1 are necessary to further our understanding of the physics of the radiative shocks present there. Resolving the profile of the N v λ1240 and other UV lines will provide critical tests of the radiative shock model.

11. Observations and modeling of the emission-line spectra of the other spots now appearing in the ring will provide vital clues to resolving the uncertainties of the present model for spot 1. Observations with *HST*/STIS are required to spatially resolve their individual spectra.

We thank Dan Welty for sharing with us the high-resolution *IUE* observations of SN 1987A, Kailash Sahu for sending us the most recent STIS LSF, John Raymond for providing us with his radiative shock code, and John Blondin for use of his VH-1 code and his help with hydrodynamic simulations for this paper. Support for this work was provided by NASA through grant GO-08243 from the Space Telescope Science Institute, which is operated by the Association of Universities for Research in Astronomy, Inc., under NASA contract NAS 5-26255. Additional support was provided by NASA through grants NAG 5-3313 and NTG 5-80 to the University of Colorado. C. S. J. P. acknowledges funding by the STIS IDT through the National Optical Astronomy Observatories. A. V. F. is grateful for a Guggenheim Foundation Fellowship.

REFERENCES

Baron, E., et al. 2000, ApJ, 545, 444
Beuermann, K., Brandt, S., & Pietsch, W. 1994, A&A, 281, L45
Bionta, R. M., et al. 1987, Phys. Rev. Lett., 58, 1494
Blades, J. C., Wheatley, J. M., Panagia, N., Grewing, M., Pettini, M., & Wamsteker, W. 1988, ApJ, 334, 308
Blinnikov, S., Lundqvist, P., Bartunov, O., Nomoto, K., & Imamoto, K. 2000, ApJ, 532, 1132
Blondin, J. M., & Lundqvist, P. 1993, ApJ, 405, 337
Böhm, K.-H., & Goodson, A. 1997, in IAU Symp. 182, Herbig-Haro Flows and the Birth of Low Mass Stars, ed. B. Reipurth & C. Bertout (Dordrecht: Kluwer), 47
Borkowski, K., Blondin, J., & McCray, R. 1997a, ApJ, 476, L31
———. 1997b, ApJ, 477, 281
Burrows, C. J., et al. 1995, ApJ, 452, 680
Burrows, D. N., et al. 2000, ApJ, 543, L149
Cardelli, J. A., Clayton, G. C., & Mathis, J. S. 1989, ApJ, 345, 245
Cargill, P. J., & Papadopoulos, K. 1988, ApJ, 329, L29
Chevalier, R. A., & Dwarkadas, V. V. 1995, ApJ, 452, L45
Chevalier, R. A., & Imamura, J. N. 1982, ApJ, 261, 543
Chugai, N. N., Chevalier, R. A., Kirshner, R. P., & Challis, P. M. 1997, ApJ, 483, 925
Colella, R., & Woodward, P. R. 1984, J. Comput. Phys., 54, 174
Cox, D. P., & Raymond, J. C. 1985, ApJ, 298, 651
Crotts, A., & Heathcote, S. 2000, ApJ, 528, 426
Cumming, R. J., & Lundqvist, P. 1997, in Advances in Stellar Evolution, ed. R. T. Rood (Cambridge: Cambridge Univ. Press), 297
Ensman, L., & Burrows, A. 1992, ApJ, 393, 742
Fitzpatrick, E. L. 1986, AJ, 92, 1068
———. 1999, PASP, 111, 63
Fitzpatrick, E. L., & Walborn, N. R. 1990, AJ, 99, 1483
Fransson, C., Cassatella, A., Gilmozzi, R., Kirshner, R. P., Panagia, N., Sonneborn, G., & Wamsteker, W. 1989, ApJ, 336, 429
Gaensler, B. M., Manchester, R. N., Staveley-Smith, L., Tzioumis, A. K., Reynolds, J. E., & Kesteven, M. J. 1997, ApJ, 479, 845
Garnavich, P., et al. 2001, ApJL, submitted
Garnavich, P., Kirshner, R., & Challis, P. 1997, IAU Circ. 6710
———. 2000, IAU Circ. 7360
Gorenstein, P., Hughes, J. P., & Tucker, W. H. 1994, ApJ, 420, L25
Hasinger, G., Aschenbach, B., & Trümper, J. 1996, A&A, 312, L9
Hester, J. J., Danielson, G. E., & Raymond, J. C. 1986, ApJ, 303, L17
Hirata, R., et al. 1987, Phys. Rev. Lett., 58, 1490
Imamura, J. N., Wolff, M. T., & Durisen, R. H. 1984, ApJ, 276, 667
Innes, D. E. 1992, A&A, 256, 660
Innes, D. E., Giddings, J. R., & Falle, A. E. G. 1987, MNRAS, 226, 67
Jakobsen, P., et al. 1991, ApJ, 369, L63
Lawrence, S. S., Sugerman, B. E., Bouchet, P., Crotts, A. P. S., Uglesich, R., & Heathcote, S. 2000a, ApJ, 537, L123
Lawrence, S. S., Sugerman, B. E., & Crotts, A. P. S. 2000b, IAU Circ. 7419
Leitherer, C., et al. 2000, STIS Instrument Handbook, Version 4.0 (Baltimore: STScI), 343
Lentz, E. J., et al. 2001, ApJ, 547, 406
Link, R., Rosenberg, D. L., & Chevalier, R. A. 2002, in ASP Conf. Ser. 260, Interacting Winds from Massive Stars, ed. A. F. J. Moffat & N. St-Louis (San Francisco: ASP), in press
Long, K. S., & Blair, W. P. 1990, ApJ, 358, L13
Lundqvist, P. 1999, ApJ, 511, 389
Lundqvist, P., & Fransson, C. 1991, ApJ, 380, 575
Lundqvist, P., & Fransson, C. 1996, ApJ, 464, 924
Lundqvist, P., & Sonneborn, G. 2001, in ASP Conf. Ser., SN 1987A: Ten Years After, ed. M. Phillips & N. Suntzeff (San Francisco: ASP), in press
Luo, D., & McCray, R. 1991, ApJ, 379, 659
Luo, D., McCray, R., & Slavin, J. 1994, ApJ, 430, 264
Manchester, R. N., Gaensler, B., M., Wheaton, V. C., Staveley-Smith, L., Tzioumis, A. K., Bizunok, N. S., Kesteven, M. J., & Reynolds, J. E. 2002, Proc. Astron. Soc. Australia, 19, 207
Maran, S. P., Sonneborn, G., Pun, C. S. J., Lundqvist, P., Iping, R., & Gull, T. R. 2000, ApJ, 545, 390
Martin, C., & Arnett, W. D. 1995, ApJ, 447, 378
Masai, K., & Nomoto, K. 1994, ApJ, 424, 924
Michael, E., et al. 1998a, ApJ, 509, L117
———. 2000, ApJ, 542, L53
Michael, E., McCray, R., Borkowski, K. J., Pun, C. S. J., & Sonneborn, G. 1998b, ApJ, 492, L143
Osterbrock, D. E. 1989, Astrophysics of Gaseous Nebulae and Active Galactic Nuclei (Mill Valley: University Science Books)
Panagia, N., Romaniello, M., Scuderi, S., & Kirshner, R. P. 2000, ApJ, 539, 197
Park, S., Burrows, D. N., Garmire, G. P., Nousek, J. A., McCray, R., Michael, E., & Zhekov, S. 2002, ApJ, 567, 314
Plait, P. C., Lundqvist, P., Chevalier, R. A., & Kirshner, R. P. 1995, ApJ, 439, 730
Pun, C. S. J., et al. 1995, ApJS, 99, 223
Ramsbottom, C. A., Berrington, K. A., Hibbert, A., & Bell, K. L. 1994, Phys. Scr., 50, 246
Raymond, J. C. 1979, ApJS, 39, 1
Russell, S. C., & Dopita, M. A. 1992, ApJ, 384, 508
Scuderi, S., Panagia, N., Gilmozzi, R., Challis, P. M., & Kirshner, R. P. 1996, ApJ, 465, 956
Seaton, M. J. 1979, MNRAS, 187, 73P
Sonneborn, G., et al. 1997, ApJ, 477, 848
———. 1998, ApJ, 492, L139
Staveley-Smith, L., Briggs, D. S., Rowe, A. C. H., Manchester, R. N., Reynolds, J. E., Tzioumis, A. K., & Kesteven, M. J. 1993, Nature, 366, 136
Staveley-Smith, L., et al. 1992, Nature, 355, 147
Strickland, R., & Blondin, J. M. 1995, ApJ, 449, 727
Suzuki, T., Shigeyama, T., & Nomoto, K. 1993, A&A, 274, 883
Tielens, A. G. G. M., McKee, C. F., Seab, C. G., & Hollenbach, D. J. 1994, ApJ, 431, 321
Walborn, N. R., Phillips, M. M., Walker, A. R., & Elias, J. H. 1993, PASP, 105, 1240
Walder, R., & Folini, D. 1998, A&A, 330, L21
Walker, A. R., & Suntzeff, N. B. 1990, PASP, 102, 131
Wampler, E. J., Richichi, A., & Baade, D. 1989, in IAU Colloq. 120, Structure and Dynamics of the Interstellar Medium, ed. G. Tenorio-Tagle, M. Modes, & J. Melnick (Berlin: Springer), 190
Wang, L. 1991, A&A, 246, L69
Wang, L., et al. 1996, ApJ, 466, 998
Welty, D. E., Frisch, P. C., Sonneborn, G., & York, D. G. 1999, ApJ, 512, 636
Zeldovich, Ya. B., & Raizer, Yu. P. 1967, Physics of Shock Waves and High-Temperature Hydrodynamic Phenomena (New York: Academic Press)